Radiation-Induced Effects on Materials Properties of Ceramics: Mechanical and Dimensional Properties

Kazuhiro Yasuda, Jean-Marc Costantini, Gianguido Baldinozzi

12052 Radiation-Induced Effects on Materials Properties of Ceramics: Mechanical and Dimensional Properties[☆☆]

Kazuhiro Yasuda, Kyushu University, Fukuoka, Japan

Jean-Marc Costantini, and Gianguido Baldinozzi, University of Paris-Saclay, Gif-sur-Yvette Cedex, France

Nomenclature

BF Bright-Field
BZ Brillouin Zone
DOS Density-of-states
dpa Displacement per atom
E_d Threshold Displacement Energy
EELS Electron Energy Loss Spectroscopy
EPR Electron Paramagnetic Resonance
E-SEM Environmental Scanning Electron Microscopy
EXAFS Extended X-ray Absorption Fine Structure
EXELFS EXtended Energy-Loss Fine Structure
fcc Face-centered cubic
FF Fission Fragment
FTIR Fourier Transform Infrared
HAREXCS High Angular Resolution Electron Channeling X-ray Spectroscopy
HBS High Burnup Structure
HRTEM High Resolution Transmission Electron Microscopy
IMF Inert Matrix Fuel
IR Infrared Radiation
LA Longitudinal Acoustical

LLFP Long Life Fission Product
LO Longitudinal Optical
LRO Long Range Order
SRO Short Range Order
LWR Light Water Reactor
MD Molecular Dynamics
MSDA Multi-Step Damage Accumulation
NN Nearest-Neighbors
RBS/C Rutherford Backscattering Spectroscopy/Channeling
RDF Radial Distribution Function
RRI Relative Raman intensity
SHI Swift HeavyIon
SOFC Solid Oxide Fuel Cell
STEM Scanning Transmission Electron Microscopy
TA Transverse Acoustical
TEM Transmission Electron Microscopy
TO Transverse Optical
UV Ultra-Violet
XPS X-ray Photoelectron Spectroscopy
XRD X-ray Diffraction
YSZ Yttria Stabilized Zirconia

1 Introduction

Energetic particles, such as fast neutrons, ions, and electrons, lose their kinetic energy in matter either through elastic or inelastic interactions: the elastic interaction with the atomic nuclei induces elastic (or ballistic) displacement damage of lattice atoms when the transferred energy exceeds the threshold displacement energy (E_d), and the inelastic interaction excites orbital and core electrons and ionize lattice atoms.[1,2] It should be noted in ceramic compounds that point defects and extended defects are induced by both elastic and inelastic interactions.[3] Also, the kinetic behavior of point defects and formation of extended defects are strongly influenced by the inelastic interactions with energetic particles.

Many ceramics are polyatomic compounds, except for some monoatomic materials, such as Si, Ge and graphite. The unit cells of ceramic compounds are, in general, larger than metallic materials, and they are composed of sublattices of the constituent ions. The values of E_d can be different on each sublattice, and this causes the unbalance of the production rate of point defects. The bonding of ceramics is ionic and/or covalent: the fraction of bonding nature can be expressed by ionicity, such as for Pauling' ionicity and Phillip-Van Vechten's iconicity.[4] For examples, the value of Phillips ionicity is evaluated to be 0.73 for MgO (most entirely ionic) and 0.18 for SiC (most entirely covalent). More recent analysis has dealt with the charge density distribution around and in between atoms so as to define a true ionic/covalent character of chemical bonds.[5] Ceramics with lower values of ionicity are known to be easily amorphized by energetic particle irradiation.[6,7] Molecular dynamics (MD) simulations on a variety of ionic-covalent solids have indeed highlighted the importance of bond character in the response to displacement damage.[8] As an additional feature, many of ceramic compounds exist in a wide range of composition as non-stoichiometric compounds. In such a case, structural vacancies (or empty interstitial sites) are induced in a corresponding sublattice to preserve the charge neutrality. The charge states of point defects are also important to influence the migration energy of the defects and the stability of defects. Synergistic effects of elastic nuclear displacement and electronic excitation are known to influence the kinetics of defect formation and microstructure evolution in ceramics.[9–14] It is also important to note that the charge state of point defects may change due to the charge transfer between ions as a function of time under electronic excitation.[3,15] Some MD simulations have actually tried to take into account the charge transfer between recoiling atoms during collision cascades in SiC leading to the formation of charged defects.[16] As described above, there are several additional factors, compared to metallic materials, to be considered for the radiation damage in ceramics, thereby the radiation damage process in ceramics is more complex. As a result, it turns out that this process is not fully understood at present.

In this article, we have selected three types of ceramic compounds: (1) fluorite-type oxides (such as yttria stabilized cubic zirconia (YSZ), urania, and ceria), (2) silicon carbide, and (3) normal spinel structure oxides (such as magnesium aluminate spinel). All of those materials are of importance for nuclear applications, such as for inert matrix nuclear fuel (IMF), transmutation target, nuclear waste, electrical and optical materials for fusion devices, and so on. Moreover, those materials have a different nature of bonding: silicon carbide is mostly covalent, whereas zirconia and magnesium aluminate spinel are mostly ionic. Further, silicon carbide is known as an amorphizable material and fluorite-type oxides are strongly resistant to amorphization.

As mentioned in the title of this article, we describe the dimensional stability and mechanical properties of these characteristic and important ceramics. It is needless to say that the dimensional stability is directly related to the defect production, kinetics, and microstructure evolution, especially for the accumulation of point defects and void swelling. Also, mechanical properties are highly sensitive to the change in microstructure caused by irradiation. However, mechanical properties of ceramic compounds, especially for neutron irradiated specimens, have not been fully investigated. Limited investigations were reported such as for the dimensional change, flexural bend bar tests and fracture toughness measurements.[17–21] This is based on the fact that the ability for plastic deformation of ceramics is significantly low (or Peierls barriers for dislocation motion is high), which requires high temperatures for mechanical testing. Further, measurements of mechanical properties are inevitably limited to the surface region (typically 1 µm or less) if ion-irradiated specimens are tested. Development of miniaturized specimen techniques for mechanical testing has been an important topic not only for ceramics, but also for metals, due to the small available volume of the limited number of nuclear testing reactors and the use of ion irradiation.[22] The availability of those techniques for ceramics is, however, limited mostly to indentation measurements due to their brittleness mentioned above. For this reason, most of investigations on the mechanical properties of irradiated materials are devoted to nano-indentation measurements. Analysis on the continuous of loading and unloading curves during indentation process allows to obtain elastic (Young's modulus) and plastic (hardness) properties of materials.[23] Indentation depth was controlled to keep around 20%–30% thickness of the damaged region to detect hardness itself of the thin surface layer (or damaged layer with ions).[24]

It is worthwhile to note that there are excellent books and reviews for radiation effects in ceramics.[12,15,25–30] Thanks to the achievements of those articles, we will review the defect production, migration, formation of extended defects, accumulation of defects of those three types of ceramic compounds (that is, fluorite-type oxides, silicon carbide and magnesium aluminate spinel), with emphasizing the similarity and difference of these materials, to lead to the discussion on the dimensional stability and mechanical properties of ceramics.

2 Fluorite-Type Oxides

2.1 Introduction

Extensive investigations have revealed that fluorite-type oxides, such as yttria-stabilized cubic zirconia (ZrO_2: Y, or YSZ), ceria (CeO_2) and urania (UO_2) are exceptionally resistant to radiation damage. UO_2 has shown excellent performance for years as nuclear fuels in light

water reactors (LWRs), and YSZ has potential applications, such as IMF for burning excess plutonium and transmutation target of long lived fission products (LLFPs).[31–33] A composite of fluorite-type oxides and magnesium aluminate spinel ($MgAl_2O_4$) was also proposed for IMF and a nuclear waste form.[34,35] On the other hand, ceria has been used as a surrogate material for the basic studies of PuO_2 and UO_2,[36–44] since both Ce and Pu atoms share the 3+ and 4+ oxidation states, and their dioxides have the same cubic-fluorite crystal structure. To date, however, the stability of these dioxides under irradiation is not fully understood and the details of their radiation response still remains as an open question.

Fig. 1 shows the fluorite structure, in which cations form face centered cubic (fcc) structure and oxygen ions occupy the eight tetrahedral sites in a unit cell.[45] It is noted that fluorite-type oxides reveals non-stoichiometric (hypo- and hyper-nonstoichiometric) compositions, such as $UO_{2 \pm x}$, $CeO_{2 - x}$, and YSZ contains structural vacancies in the cation sublattice to keep the charge neutrality due to the solution of Y^{3+} ions at Zr^{4+} sites. The non-stoichiometry strongly influences the kinetic behavior of point defects and physical properties of fluorite-type oxides, in particular for SOFC (Solid Oxide Fuel Cell) applications. An extensive review was already published in a recent book about fluorite-like structure oxides, with an emphasis on point defect formation and recovery in YSZ by electron and ion irradiations in a wide energy range on the basis of electron paramagnetic resonance (EPR) spectroscopy and optical spectroscopy,[46] and actinide compounds with fluorite structure.[47] However, a more comprehensive review is needed to include new data on ceria and urania in order to highlight the similarities between these dioxides. In this section, the threshold displacement energy, the aggregation to extended defects under nuclear and electronic energy loss, non-stoichiometry and oxidation of UO_2, structural stability of nano-sized ZrO_2, and the dimensional stability and mechanical properties of fluorite-type oxides are reviewed.

2.2   Displacement Energy of Cations and Anions in Fluorite-Type Oxides

The displacement energy (E_d) of constituent ions is one of the most important parameter to describe radiation effects in ceramic compounds, and values of E_d in some limited ceramic compounds were summarized in review papers.[12,30,48] A number of experimental and theoretical evaluations of E_d were reported for fluorite-type oxides, such as by optical measurements, transmission electron microscopy (TEM), EPR, empirical MD and ab initio MD simulations.[41,43,49–55] Table 1 summarizes the reported E_d values of several fluorite-type oxides for cations and oxygen ions. Although the values of E_d depend on materials, crystallographic orientations and
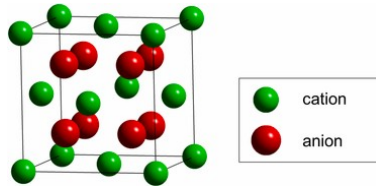

Fig. 1 Schematic of the fluorite crystal structure. Cations form face centered cubic (fcc) structure and oxygen ions occupy the tetrahedral sites in the fcc unit cell.

Table 1   Displacement energies for cation and anions in fluorite-type oxides

Material	Threshold displacement energy, E_d (eV)		Method	Reference
	Cation	Anion		
UO_2	~ 40	~ 20	HVEM	**39**
	35–51	–	MD Simulation	**40**
	43–85	16–28	MD Simulation	**41**
ThO_2	48.5 – 61.5	17.5 –>100	ab initio MD	**42**
CeO_2	44≪58	<33	HVEM	**33**
	56	27	MD Simulation	**31**
	46–63	20–33.5	ab initio MD	**42**
ZrO_2	54–68.5	14–100	ab initio MD	**42**
YSZ	80	120	EPR	**43**
	80	>200	MD Simulation	**44**
	66–89	–	HVEM	**45**

evaluation techniques, the values of E_d for cations in fluorite oxides are approximately within the range of 50–80 eV, and those of oxygen ions are around 30 eV. Namely, the value of E_d for cations is approximately twice larger than that of oxygen ions. On the other hand, a large E_d value (> 120 eV) was deduced for oxygen ions in electron-irradiated YSZ from EPR data on F$^+$ centers (paramagnetic oxygen vacancies), which is in good agreement with the MD simulations.[53] The larger value of the E_d for oxygen ions in YSZ is not cleared at the present moment. An explanation for this discrepancy is due to the promoted recombination of oxygen interstitials with structural oxygen vacancies induced by the addition of Y^{3+} dopants. The recombination pathways of Frenkel defects were investigated by MD simulations for CeO$_2$[41,56] and UO$_2$[57] Oxygen interstitials recombine spontaneously in a short time (~0.1 ps) with oxygen vacancies up to a distance of third nearest neighbors (3NNs), and for longer distances the recombination was found to take place by the thermally activated migrations through the replacement with an oxygen ion in a lattice position along the [100] direction.[41,56]

In general, cations in fluorite-type oxides are, significantly heavier than oxygen ions. The transferred kinetic energies from energetic particles, therefore, become larger for oxygen than cation. This influence can be obvious if the mass of radiation particle is in the light case, such as for electrons.[53,58] Elastic displacement cross sections with electron irradiation can be calculated by using Oen's chart[59] based on McKinley-Feshbach formula,[60] or a computer code (SMOTT/POLY) on the basis of Mott cross sections.[61] The SMOTT/POLY code is devised to include the cascade contributions for polyatomic species. Namely, cross sections are totally calculated including additional displacements induced by all recoil species. **Fig. 2** is an example of elastic displacement cross sections obtained by SMOTT/POLY for O and Zr ions in YSZ with various E_d values.[53] **Fig. 2** shows that the displacement damage is induced selectively or preferentially on oxygen ions up to an electron energy of around 1 MeV. This influences the nature of defects and microstructure evolution in fluorite-type oxides, which will be described in the latter section.

2.3   Radiation-Induced Defects and Microstructure Evolution

2.3.1   *Effects of displacement damage*

Damage accumulation in stabilized cubic zirconia was investigated by in situ Rutherford backscattering spectroscopy/Channeling (RBS/C) measurements at low temperatures (**Fig. 3**)[33,62,63] Damage accumulation parameter, χ, was plotted as a function of 400 keV Xe-ion fluence for fully stabilized cubic zirconia contained either Y$_2$O$_3$, CaO or Er$_2$O$_3$, in which values of χ reveals progressive evolution with three distinct stages against Xe-ion fluence. A TEM investigation [63] showed that tiny (< 5 nm in diameter) isolated defect clusters were formed at stage I and dislocation loops and dislocation networks were observed at stage III. The sudden increase of χ at stage II was interpreted by the change in the scattering process of the He-ion probe for RBS/C measurements from the direct scattering to the deflection due to the lattice distortion.[63] It is noted that the values of χ do not reach a value of unity at high fluence. Namely, the stabilized cubic zirconia crystals do not amorphize under irradiation at a low temperature of 170K to a high dose level of 100 displacement per atom (dpa), indicating the high resistance of stabilized cubic zirconia to amorphization and excellent dimensional stability. On the other hand, MgAl$_2$O$_4$ has exhibited a transition to amorphous state at the equivalent condition.[33] The microstructure evolution and mechanism for the radiation stability in MgAl$_2$O$_4$ will be described in **Section 4**.
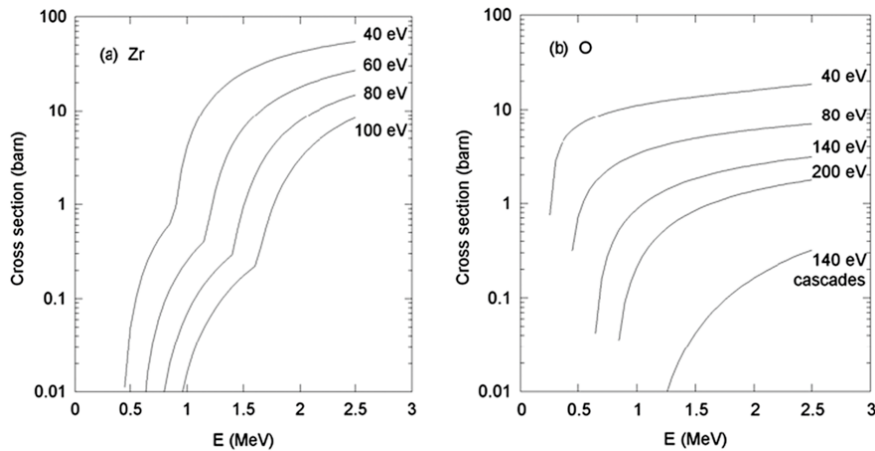

Fig. 2 Calculated displacements cross section for (a) Zr- and (b) O-sublattice in zirconia by using SMOTT/POLY code as a function of electron energy with various E_d values. For O ions with E_d = 140 eV, both total cross section and cascade contributions are given. Reproduced with permission from Costantini, J.-M., Beuneu, F., 2007. Phys. Status Solidi (c) 4 (3), 1258–1263.
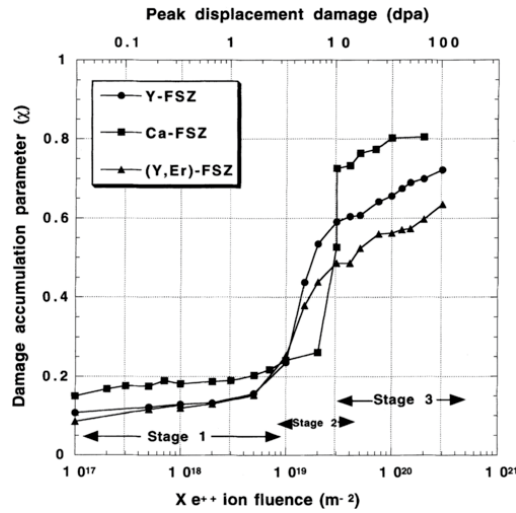
Fig. 3 Damage accumulation parameter, χ, in fully-stabilized cubic zirconia by in situ RBS/C experiments as a function of Xe-ion fluence. Irradiation was performed with 400 keV Xe ions at 170K. Values of dpa at the corresponding ion fluence is shown on the upper abscissa. Y-FSZ, Ca-FSZ and (Y, Er)-FSZ represent single crystal specimens stabilized with 9.5 mol% Y_2O_3, 14.1 mol% CaO, and 11.1 mol% Y_2O_3 and 1.3 mol% Er_2O_3, respectively. Reproduced with permission from Sickafus, K.E., Matzke, H., Hartmann, T., *et al.*, 1999. J. Nucl. Mater. 274 (1–2), 66–77.

Damage accumulation was also investigated in detail with hundreds keV and to MeV heavy ions. **Fig. 4** shows the accumulation of maximum damage fraction (f_D^{max}) and elastic strain (ε_n^{max}) in YSZ irradiated with 4 MeV Au ions obtained by RBS/C and X-ray diffraction (XRD) measurements, respectively, together with the corresponding TEM images.[64,65] The accumulation of f_D^{max} and ε_n^{max} was reproduced by a multi-step damage accumulation (MSDA) model[66] and was interpreted with the similar progress with ion fluence described above. The decrease in f_D^{max} and ε_n^{max} at high fluence was attributed to the formation of dislocation networks. Interestingly, irradiations to high fluence with a few hundred keV Cs ions were found to induce a transition to amorphous state at room temperature, due to the stabilization of lattice disorder by the presence of chemically active impurities.[66–68] Microstructure evolution was also reported to reveal, such as grain growth[69] and Xe bubble formation with 60 keV Xe ions at 1073K at high fluence of 3×10^{16} cm^{-2}.[70] The transition to amorphous state was, however, not reported due to the solely accumulation of displacement damage.

As described in the previous section (**Section 2.2**), the selective irradiation damage of oxygen ions under electron irradiation induces different types of defects in fluorite-type oxides dependent on electron energy. F$^+$-type centers (namely oxygen divacancy defects) were detected in electron-irradiated YSZ by EPR spectroscopy and UV–visible absorption spectroscopy.[71] **Fig. 5** shows the growth process of defects in YSZ recorded by in situ TEM under 200 keV electron irradiation (corresponding to the selected displacement damage condition on oxygen ions), which shows a unique and significantly different growth process from the perfect dislocation loops.[58] The loop with strong diffraction contrast grows with electron irradiation time (from a to d) and suddenly changes the contrast to dislocation lines (from d to e). Namely, segments of dislocations were multiplied from the defect (e), and continuous electron irradiation produced new several defects preferentially at or near dislocation lines and followed the same growth process (f to j). Similar defects with strong diffraction contrast were observed in fluorite-type compounds of CeO$_2$ [43,72] and CaF$_2$.[73] These defects were discussed to be non-stoichiometric dislocation loops consist of oxygen ions lying on {111} planes from TEM analysis[58,72] atomic resolution scanning TEM (STEM) observations[74] and MD simulations.[56] Selectively displaced charged oxygen ions were discussed to aggregate on {111} planes accompanying strong strain field. Analysis on rate theory equations with taking internal charge accumulation due to the aggregation of negatively charged oxygen ions revealed the presence of significantly large strain field around the defects, which was equivalent to multiply dislocations as observed in **Fig. 5(e)**.[75] Electron irradiation in CeO$_2$ with 2 and 3 MeV, where both Ce and O ions are displaced, was shown to induce perfect-type dislocation loops with stoichiometric composition.[43] Consequently, the selective displacement damage on oxygen sublattice significantly influences the defect kinetics, the nature of defects and the local charge accumulation in fluorite-type compounds. Recovery of F$^+$-type centers after electron or ion irradiations was observed by UV–visible absorption spectroscopy after thermal annealing at 523K with first-order kinetics,[76] which is good agreement with the nucleation threshold temperature for the non-stoichiometric oxygen dislocation loops.[58] Almost full bleaching was also obtained by laser illumination in the absorption band of F$^+$ centers for a wavelength of ~550 nm.[76]
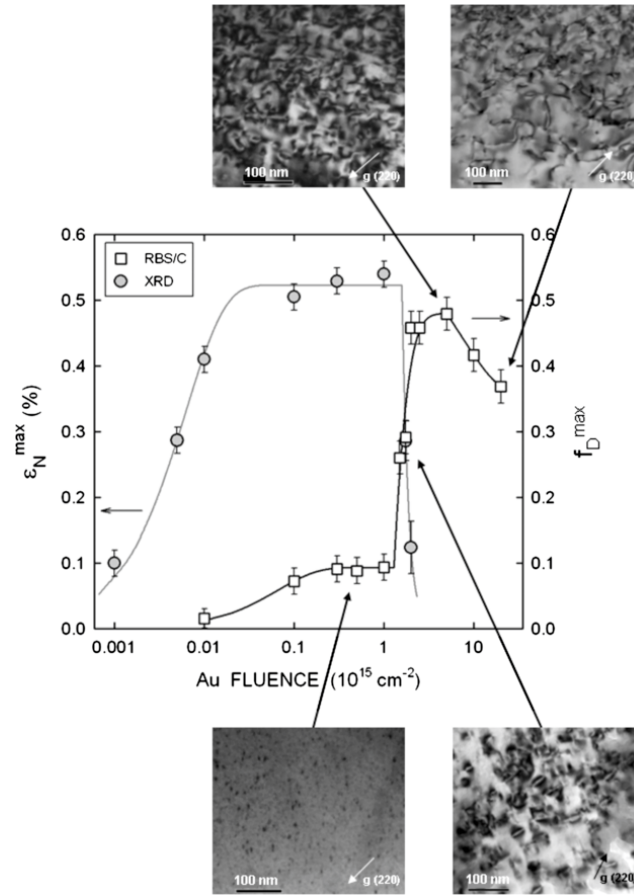
Fig. 4 Maximum damage fraction ($f_D{}^{max}$) and elastic strain ($\varepsilon_n{}^{max}$) in YSZ single crystals (9.5 mol% Y$_2$O$_3$) obtained from RBS/C and XRD as a function of 4 MeV Au ions. TEM images showing dot contrast, dislocation loops and dislocation networks are inserted to the corresponding data points. Lines are derived from the multi-step damage accumulation model. Reproduced with permission from Moll, S., Thomé, L., Sattonnay, G., *et al.*, 2009. J. Appl. Phys. 106 (7), 073509. Shiiyama, K., Yamamoto, T., Takahashi, T., *et al.*, 2010. Nucl. Instrum. Methods B 268 (19), 2980–2983.

2.3.2 Effects of high density electronic excitation by swift heavy ions

Radiation damage with high density electronic excitation is also important for nuclear materials, since it relates to radiation damage with fission fragments (FFs) with energies around 70 MeV and 100 MeV.[77] Investigations with swift heavy ion (SHI) irradiation with energies around 70 MeV to GeV were extensively performed to mimic radiation damage with FFs (the electronic energy loss of FFs reaches around 20 keV/nm), and to gain insights into the radiation damage mechanism with high density electronic excitation.

SHI irradiation induces ion tracks in CeO$_2$,[37,78,79] YSZ [80] and UO$_2$.[81] **Fig. 6** shows examples of ion tracks, showing bright-field (BF) TEM images of ion tracks in CeO$_2$ irradiated with 210 MeV Xe ions to a fluence of 1×10^1 cm^{-2}. The core regions of ion tracks appeared as Fresnel contrast, where contrast of ion tracks reverse black (over-focus condition) and white (under-focus condition) depending on the focus condition. Fresnel contrast together with high resolution TEM (HRTEM) images of ion tracks deduced that ion tracks in fluorite-type oxides keep the fluorite structure, whereas the atomic density inside the core region of ion tracks (typically ~3 nm in diameter) is decreased.[78,79] The decrease in the atomic density was evaluated to be 13% from a thickness fringe analysis of TEM images for the case of
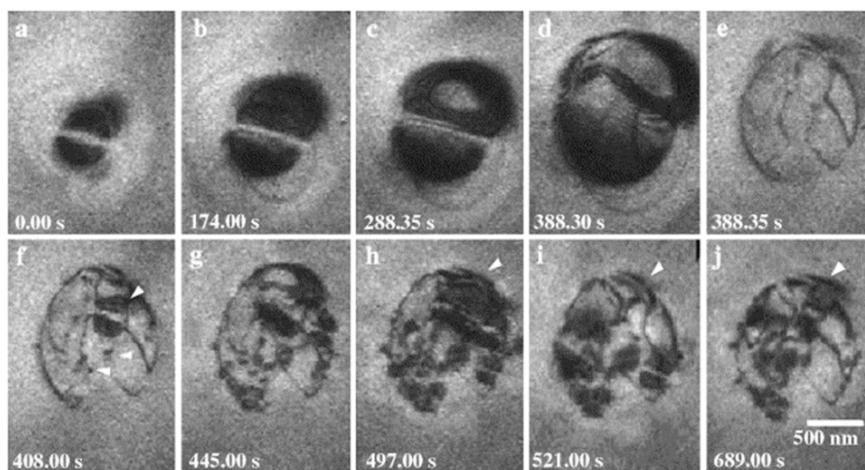
Fig. 5 Growth process of non-stochiometric dislocation loops lying on {111} planes in YSZ under 200 keV electron irradiation at 470K, which were considered to be charged dislocation loops with an additional oxygen layer between oxygen {111} planes. The specimen was irradiated originally with 300 keV O^+ ions at 470K to a fluence of 5.1×10^{13} cm^{-2} followed by a focused electron beam (electron flux at the center of the beam was $\sim 10^{19}$ cm^{-2} s^{-1}) at 470 K to nucleate the defect cluster (a). Real electron-irradiation time from the microstructure of (a) is shown at each photo with an electron flux of $\sim 5 \times 10^{17}$ cm^{-2} s^{-1}. The diffraction vector is $g = 220$. The arrow in (f) reveals the nucleation of defects with same nature of (a) at a line dislocation, following the repeats of growth and conversion to dislocation line (f to j). Reproduced with permission from Yasuda, K., Kinoshita, C., Matsumura, S., Ryazanov, A.I., 2003. J. Nucl. Mater. 319, 74–80.
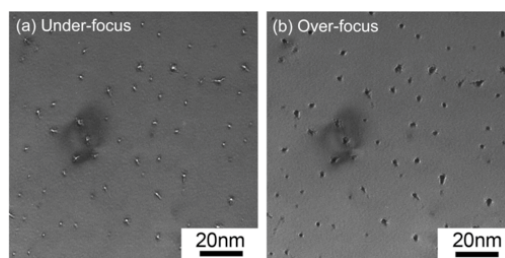

Fig. 6 Plan-view microstructures from BFTEM images of an identical region in CeO_2 irradiated at ambient temperature with 210 MeV Xe ions to a fluence 1×10^{12} cm^{-2}, taken with a kinematical diffraction condition with under-focus (a) and over-focus (b) conditions to observe the core damage regions of ion tracks with Fresnel-contrast. Reproduced with permission from Yasuda, K., Etoh, M., Sawada, K., *et al.*, 2013. Nucl. Instrum. Method B 314, 185–190.

CeO_2 irradiated with 200 MeV Xe ions.[79] **Fig. 7** is an atomic resolution STEM image of an ion track in CeO_2 irradiated with 200 MeV Xe ions to a fluence of 3×10^{12} cm^{-2}. An ion track exists at the center part of **Fig. 7** at nearly an end-on condition. Analysis on the signal intensity profile confirmed that the fluorite structure is kept inside the ion track, although the atomic density is decreased and oxygen sublattice is disordered preferentially. It is also shown that the sharp Raman-active T_{2g} phonon mode of the fluorite structure at 467 cm^{-1} exhibits a peculiar asymmetrical peak after heavy ion irradiations of CeO_2 sintered samples that may be associated to oxygen vacancy formation.[82] A weak and broad Raman peak centered at about 600 cm^{-1} was also assigned to oxygen vacancies.[82,83] Based on these results, the structure of ion tracks was discussed to be a vacancy rich region with keeping fluorite structure.[78]

Size of ion tracks in CeO_2, YSZ and UO_2 was reported by different techniques, such as RBS/Channeling,[53,65,80] XRD,[84] TEM [37,78,85–87] and Raman spectroscopy.[82] **Fig. 8** plots the ion track radii in CeO_2 derived from different techniques as a function of electronic stopping power. The size of tracks increases with electronic stopping power, and the data derived from XRD,[86] TEM,[36] and Raman data [82] agree
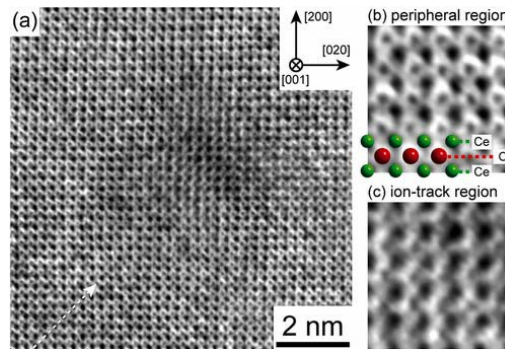
Fig. 7 High resolution annular bright-field (ABF)–scanning transmission electron microscopy (STEM) image of CeO$_2$ taken from the [0 0 1] direction (a), irradiated with 200 MeV Xe ions to 3 × 10^{12} cm^{-2}. Magnified images of the peripheral region (b) and the core damage region of the ion track (c) are also presented. The corresponding atomic configuration is superimposed on the magnified image of (b). Reproduced with permission from Takaki, S., Yasuda, K., Yamamoto, T., Matsumura, S., Ishikawa, N., 2014. Nucl. Instrum. Method B 326, 140–144.
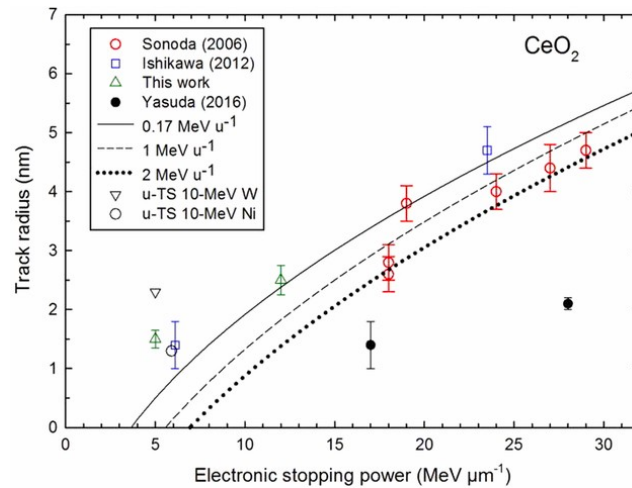

Fig. 8 Experimental radii of ion tracks in CeO$_2$ vs. electronic energy loss from Sonoda *et al.*, Ishikawa *et al.*, Takaki *et al.* and Costantini *et al.* The lines are derived from inelastic thermal spike (*i*-TS) calculations for the three different beam energies of 0.17, 1.0, and 2.0 MeV µm^{-1}. Open triangles and open circles are u-TS calculations combining the electronic and nuclear energy losses for 10-MeV W and 10-MeV Ni ions. Reproduced with permission from Costantini, J.-M., Miro, S., Gutierrez, G., *et al.*, 2017. J. Appl. Phys. 122, 205901. Ewing, R.C., Weber, W.J., Lian, J., 2004. J. Appl. Phys. 95 (11), 5949–5971. Sickafus, K.E., Kotomin, E.A., Uberuaga, B.P., 2006. Radiation effects in solids. In: Proceedings of the NATO Advanced Study Institute the 32nd Course of the International School of Solid State Physics Entitled Radiation Effects in Solids held in Erice, Sicily, Italy. July 17–29, 2004. Dordrecht: Springer. Takaki, S., Yamamoto, T., Kutsuwada, M., Yasuda, K., Matsumura, S., 2013. Adv. Mater. Nucl. Energy 1514, 93. Jagielski, J., Thomé, L., 2009. Appl. Phys. A. 97 (1), 147–155. Ryazanov, A.I., Yasuda, K., Kinoshita, C., Klaptsov, A.V., 2003. J. Nucl. Mater. 323 (2–3), 372–379. Zhang, Y., Aidhy, D.S., Varga, T., *et al*., 2014. Phys. Chem. Chem. Phys. 16 (17), 8051–8059. Costantini, J.-M., Touati, N., Binet, L., *et al*., 2018. Philos. Mag. 98 (14), 1241–1255.

well with the prediction of the inelastic thermal spike (*i*-TS) model [88] (Details of thermal spike model is also described in Chapter 1.0@ in this volume).[89] Data from TEM and STEM,[87] on the other hand, yield significantly smaller values of track core radii for the same stopping powers. This is probably due to the defocus condition and observation technique used in TEM/STEM: the size reported by Takaki *et al.*[87] presumably detected the region where the decrease in the atomic density is remarkably larger than other reports.

It is also worthy to note that SHIs recover pre-existing ion tracks within a certain region.[78] This recovery region was derived from an analysis of the accumulation process of ion tracks: an evaluation for the recovery region was reported to be 8.4 nm in radius for CeO_2 with 210 MeV Xe ions, which is significantly larger than the track size detected by TEM.[78] The density of ion tracks saturates at a fluence before the overlap of ion track regions (< 5 nm in radius detected by TEM, XRD, and RBS/C techniques) occurs. Namely, the formation and recovery of ion tracks (or a vacancy rich region) are balanced at high fluence due to the larger size of recovery region to keep a saturation density of ion tracks.[78]

SHIs also induce lattice expansion and swelling.[90,91] The saturated value of lattice expansion in YSZ with a wide range of electronic stopping power (5–48.4 keV/nm) was evaluated to be 0.2% at a dose of 0.3 dpa.[91] This is significantly smaller than those observed in SiC and α-Al_2O_3 (the swelling of SiC and α-Al_2O_3 will be described in Sections 3 and 4, respectively), and revealed the superior dimensional stability of this material. It is also interesting to note that the saturated values of lattice parameter expansion and microstrain are different between CeO_2 and ThO_2.[90] XPS (X-ray Photoelectron Spectroscopy) and EXAFS (Extended X-ray Absorption Fine Structure) investigation showed that irradiation by 200 MeV Xe ions caused the valence state of the Ce cation to change from Ce^{4+} to Ce^{3+} in order to decrease the coordination number (**Fig. 9**).[92,93] This redox reaction was discussed to attribute to the change in microstructure, such as for the micro-strain and lattice parameter.[90,92] EPR spectra of bulk single crystals of CeO_2 show sharp resonance lines below 10K that were assigned to paramagnetic Ce^{3+} ions (with the $4f^1$ electronic configuration) for electron irradiations of 1.4 and 2.5 MeV energies [94](**Fig. 10**). Under such electron irradiation conditions, a change in color from light blue to deep green was observed. UV–visible optical transmission spectra indeed show a broad absorption feature below the optical gap at about 3.2 eV. This extra optical feature was associated to the electric-dipole allowed $4f \rightarrow 5d$ electronic transitions from the mid-gap level of Ce^{3+} to the empty d states of Ce^{4+} in the conduction band of CeO_{2-x}. No such EPR lines and optical absorption feature were seen for 1.0-MeV electron irradiation, even though oxygen atoms can be displaced for such energy. Neither EPR signal nor optical absorption band of F centers was found for electron energies higher than 1.0 MeV. Moreover, EPR lines or optical absorption band of F^+ centers were not recorded unlike for YSZ.[95] As such, this cerium reduction process was associated to a displacement damage of Ce atoms.[94] A similar redox of Zr from 4+ to 3+ was found in YSZ and assigned to electronic excitation processes.[95]

Overlap of high density electronic excitation damage at high fluence results in the formation of dislocation networks, and eventually to the evolution of polygonization. A TEM study of CeO_2 irradiated with 210 MeV Xe ions at 573K to a high fluence of 1×10^{16} cm^{-2} revealed the formation of small size grains (less than 200 nm from the original size of 5 μm).[78] Also, RBS/C analysis disclosed the formation of slight disoriented grains in YSZ, suggesting the formation of low angle inclined grain boundary.[80] A similar kind of polygonization was also found for YSZ after swift heavy ion irradiations by using high resolution single crystal four-circle XRD.[96] The formation of small grains with high fluence SHIs may give an insight to the formation mechanism of high burnup structure (HBS) or "rim
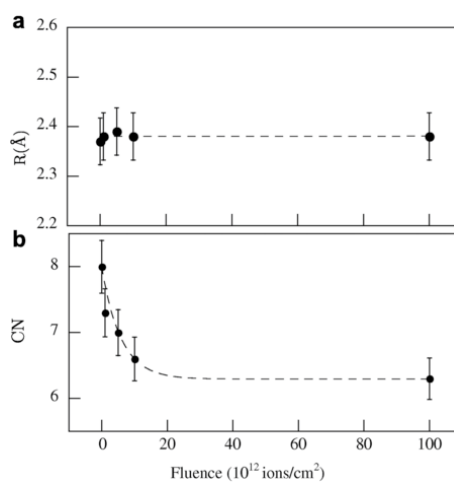

Fig. 9 Ion-fluence dependence of (a) the Ce-O interatomic distance (*R*), and (b) coordination number of Ce ions (*CN*) in CeO_2 irradiated with 200 MeV Xe ions at room temperature. Values of *R* and *CN* were obtained from an analysis of EXAFS spectra for CeO_2 thin films. Reproduced with permission from Ohno, H., Iwase, A., Matsumura, D., *et al.*, 2008. Nucl. Instrum. Method B 266 (12–13), 3013–3017.
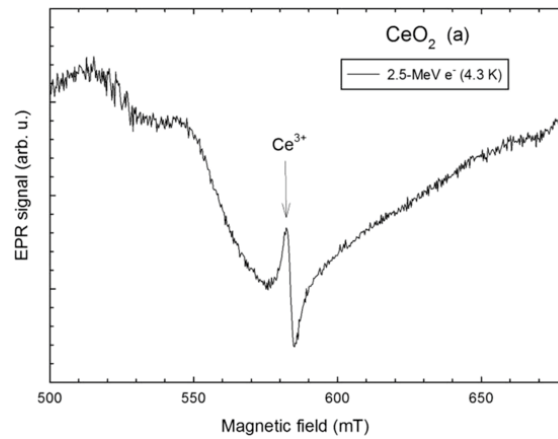
Fig. 10 X-band EPR spectrum of a 2.5-MeV electron-irradiated ceria single crystal at 4.3K. Adopted with permission from Costantini, J.-M., Miro, S., Touati, N., *et al*., 2018. J. Appl. Phys. 123 (2), 025901.

structure" in nuclear fuel,[97–99] although the real environment of nuclear fuel in a reactor is far more complicated than ion irradiation conditions. HBS in UO_2 fuel will be described in **Section 2.6**.

2.3.3 *Ferroelastic approach on the stabilization of tetragonal phase of zirconium oxides*

Zirconium oxide, ZrO_2, (and the isostructural hafnium oxide, HfO_2) can be rightly considered important ceramics not only for nuclear applications but also for very broad spectrum of functional applications (catalysis, coatings, heat shields for the space industry, additive for paints, material for oxygen probes or fuel cells, material with high dielectric permittivity (high-k) substituting for Si dioxide in MOS devices, etc.).[100–102] Many of these applications require the use of ZrO_2 in its nanometric form. The question about the fundamental mechanisms underlying tetragonal phase stabilization observed in nanocrystals but also under irradiation is then highly relevant. Indeed, the existing literature on this subject has wide divergences as regards the mechanisms leading to a significant modification of the properties of this oxide. A large number of experimental studies show that the thermodynamic properties of nanocrystalline solids can depend on particle size.

Zirconium oxide has a relatively complex phase diagram (p, T), although the crystallographic pattern is quite simple.[103–105] The mechanism of transformation from the tetragonal phase to the monoclinic phase (a semi-reconstructive phase transition) has a strong first order character, displaying a martensitic nature. The transformation occurs on cooling at about 1370K and it represents an interesting mechanical problem as there is evidence for a strong coupling between phonon softening and macroscopic strain. The tetragonal phase (**Fig. 11**), normally stable only at high temperature, can be frozen by a reduction in grain size,[106] a phenomenon also relevant for radiation-induced changes, such as those occurring in a nuclear reactor (simultaneous to cladding oxidation) or ionizing radiation encountered in the upper atmosphere or space. A coherent framework to describe these phenomena can use the generic formalism of the
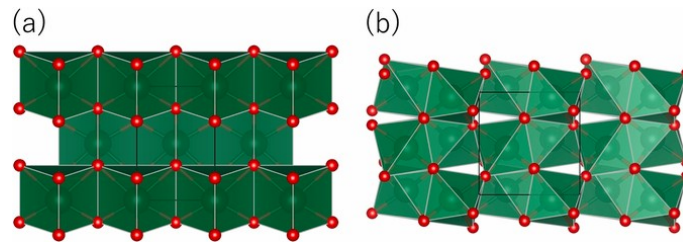

Fig. 11 Tetragonal (left panel) and monoclinic polymorphs of ZrO_2. Zr is eightfold coordinated in the tetragonal phase, and sevenfold coordinated in the monoclinic low temperature polymorph.

Landau's theory of phase transitions[107,108] to frame both the mechanism of the usual phase transitions occurring in micrometric ZrO_2 crystals and the specific behaviors proper of the nanoscale crystals.

Neutron diffraction elucidates the mechanism of this phase transition towards the low temperature monoclinic polymorph, providing evidence for the successive condensation of two phonons at the M-point on the edge of the tetragonal Brillouin zone (BZ).[109,110] Landau's formalism allows to include in a seamless way the effect of shear deformation (ε_5 using Voigt's notation) as secondary order parameter, an essential ingredient to explain the stability of the tetragonal phase in nanocrystals and the first order character of the phase transition.

Different symmetries are sometimes reported in polycrystalline ZrO_2 nanoparticles produced by techniques like spray pyrolysis. Nevertheless, monodisperse single crystallite ZrO_2 nanocrystals with initial sizes below 5 nm, obtained by several green chemistry techniques as freeze-drying or sol-gel methods, display consistently a tetragonal symmetry. In-situ neutron diffraction provide information about the lattice, the structure, the state of stress, and the evolution of the phase fractions in these nanocrystals during isothermal annealing.[111] Rietveld refinements show that the tetragonal phase of micrometric and nanometric zirconia are isostructural. The two systems can therefore be described by the same expression of the Landau free energy, with the same order parameters and the same invariants. The nanocrystal growth in isothermal annealing conditions is parabolic (surface driven) and it produces a change of the crystallite shape as they grow preferentially along the c axis direction. The growth process is accompanied by a decrease of the component ε_3 of the strain tensor according to a Laplace-type law relating strain, surface tension and crystallite size. The tetragonal phase fraction measured during the annealing can be exactly predicted by a simple model where nanocrystals exceeding a critical size of about 54 nm become monoclinic, whatever the temperature, a result experimentally observed. Indeed, the very large surface of the nanocrystals pins the secondary order parameter (elastic strain) to a fixed value which depends only on the size of the grains. The existence of a very strong coupling between the main and secondary order parameter significantly modifies the transition temperature, stabilizing the tetragonal phase in a much wider temperature range in the nanocrystals. Therefore, the critical transition temperature, which controls the evolution of the main term in the expression of the free energy of Landau, depends explicitly on the size of the grains. Strain lowers the transition temperature thus increasing the domain of stability of the tetragonal phase: below the critical size, the domain of the monoclinic phase is suppressed as the predicted transition temperature becomes negative.

This mechanical approach also explains the stabilization of the tetragonal phase in irradiated samples[62,112–118] and the phenomenon of monoclinic phase restoration after annealing as it allows to use a rate equation approach. Ion irradiation generates a non-equilibrium concentration of metastable defects[119–125] producing local strain. The spectroscopic signature of these defects and the ab-initio calculations show that the most effective defects are essentially F-type color centers. A single rate equation makes it possible to account for the transformation rates of the tetragonal phase during irradiation and annealing, without requiring more cumbersome coupling terms. The strong stress field generated by these defects couples with the main order parameter of the transition, with a term akin to the formalism used for ZrO_2 nanocrystals. Strain is now pinned by the concentration of defects and not by the surface tension. Above a given fluence (i.e., a defect concentration), the tetragonal phase is macroscopically stabilized because the effective transition temperature is lowered by the associated strain, thus stabilizing the tetragonal phase. These predictions can have important consequences because they can also help predicting the radiation effects in thin films used for instance in microelectronics when these devices are exposed to sources of ionizing radiation (cosmic rays, protons, heavy ions but also neutrons in the upper atmosphere). The problem of these nanosystems is nonetheless still very complex because the topology and geometry of the interfaces becomes important as their dimensions can match the characteristic lengths of the displacement cascades or the diameter of ion tracks: the kinetics of defect annealing and energy dissipation are then strongly affected by those interfaces,[126] that can behave as sinks for the defects, eventually leading to compensation mechanisms.

2.4   Mechanical Properties of Ion-Irradiated Zirconium Oxides

Although the mechanical properties are one of the most important physical properties for nuclear applications, only limited investigations on irradiated ZrO_2 were reported.[7,127–129] Most of the reports on the mechanical properties are based on nano-indentation measurements on ion-irradiated specimens owing to the shallow irradiated depth. Fig. 12 shows a comparison of Young's Modulus (E) between YSZ and $MgAl_2O_4$ specimens irradiated with 370 keV Xe ions at 120K.[130] Young's modulus in $MgAl_2O_4$ at a depth of 40 nm indentation increases slightly at a fluence of 1×10^{15} cm^{-2} and becomes asymptotic to around 60% of the unirradiated specimen value at high fluence. Values of E for YSZ, on the other hand, keep constant within the experimental errors up to a fluence of 1×10^{16} cm^{-2}. The decrease in Young's modulus in $MgAl_2O_4$ was discussed based on TEM observations due to the transition to amorphous state, whereas YSZ keeps its crystallinity to show a constant value of E. Values of hardness (H) showed a similar trend with Xe-ion fluence as observed in Young's modulus (Fig. 13). The hardness increases slightly at lower fluence for both YSZ and $MgAl_2O_4$ but decreases only for $MgAl_2O_4$ at high fluence. These changes in hardness are attributed to the accumulation of point defect and/or small interstitial clusters (elastic hardening), and to the amorphization for the case of $MgAl_2O_4$ (elastic softening).

2.5   Structural Analysis of Uranium Oxides Under Oxidation Conditions

The development of nuclear power plants, meeting the safety standards imposed by increasingly restrictive regulations, requires a precise knowledge of the behavior of nuclear fuel in operating, in transient, in accidental, and in storage conditions. However, the development and qualification of new fuels are long processes that span decades. For several decades, the engineering of these systems was based on empirical data without effectively including the underlying physical mechanisms. This reflects the complexity of the challenge, not only because these materials are radioactive, but also their properties are very sensitive to the chemical composition (which changes during
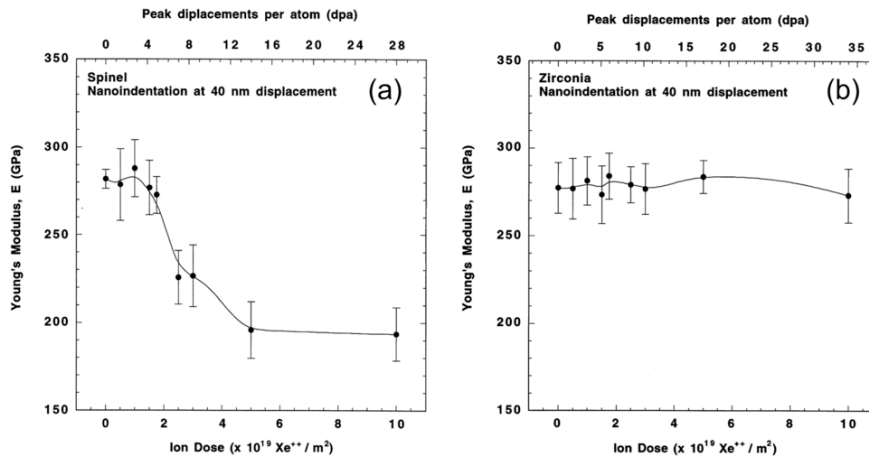
Fig. 12 Young's modulus E versus 370 keV Xe ion fluence in $MgAl_2O_4$ and YSZ irradiated at 120K at indentation depth of 40 nm. Data points represents mean values of E for ten indentations with error bars of standard deviations. The range of 370 keV Xe ions and peak dpa depth are around 70 nm and 100 nm, respectively, for $MgAl_2O_4$, and those values for YSZ are 40 nm and 80 nm, respectively. Adopted with permission from Sickafus, K.E., Wetteland, C. J., Baker, N. P., *et al.*, 1998. Mater. Sci. Eng. A 253 (1–2), 78–85.
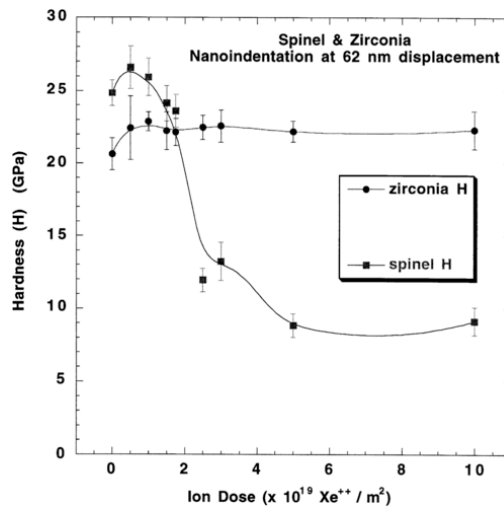

Fig. 13 Hardness, *H*, versus Xe-ion dose for spinel and zirconia crystals. Data obtained from load-displacement curves at an indenter displacement of about 62 nm. Reproduced with permission from Sickafus, K.E., Wetteland, C. J., Baker, N. P., *et al.*, 1998. Mater. Sci. Eng. A 253 (1–2), 78–85.

their life) and to the chemical potential of oxygen. In addition, they are very reactive and sensitive to changes in temperature. At present, the thermochemical and thermophysical behavior of these systems cannot be predicted by numerical techniques because some details of the electronic structure of actinides are still poorly understood. Even the problem of oxidation of UO_2, apparently simple, is a major challenge due to the complexity of the structures involved, their variety and complexity. Oxidation is among the most serious risks that

must be considered in the dry storage scenario. The UO_{2+x} system is a set of phases with quite different characteristics, ranging from fluorite structures, with an increasing number of point defects, to crystal systems where the defects can order up in more complex motifs, producing structures where crystallographic planes are reconstructed via shear mechanisms (reconstructive phase transitions) (**Fig. 14**).

During oxidation at T <600°C, UO_2 undergoes successive morphotropic transformations, with the progressive formation of U_4O_9, U_3O_7 and U_3O_8 .[131–133] Neutron diffraction studies of the isothermal kinetics of these changes (**Fig. 15**) were performed by neutron diffraction at ILL: indeed, X-ray diffraction (laboratory or synchrotron) is not very sensitive to the ordering of the defects present in the
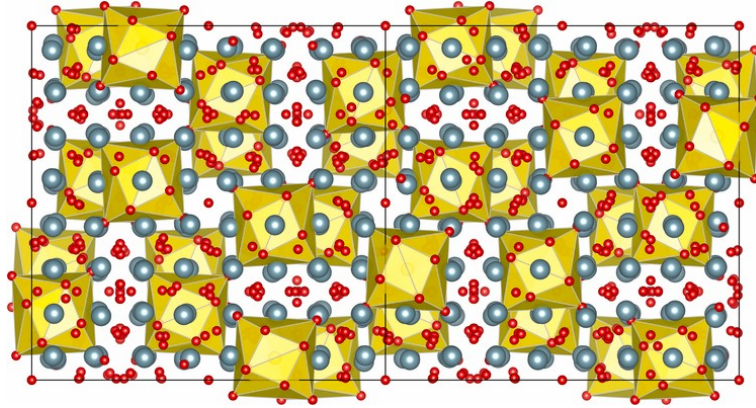

Fig. 14 Model for an antiphase boundary between two ferroelastic domains in U_3O_7. Reproduced with permission from; Whittle, K. R., Uberuaga, B.P., Bertolus, M., Grimes, R.W. *et al.*, (Eds.), 2012. Material Challenges in Current and Future Nuclear Technologies, vol. 1383. Pittsburgh, PA: Materials Research Society, pp. 35–40.
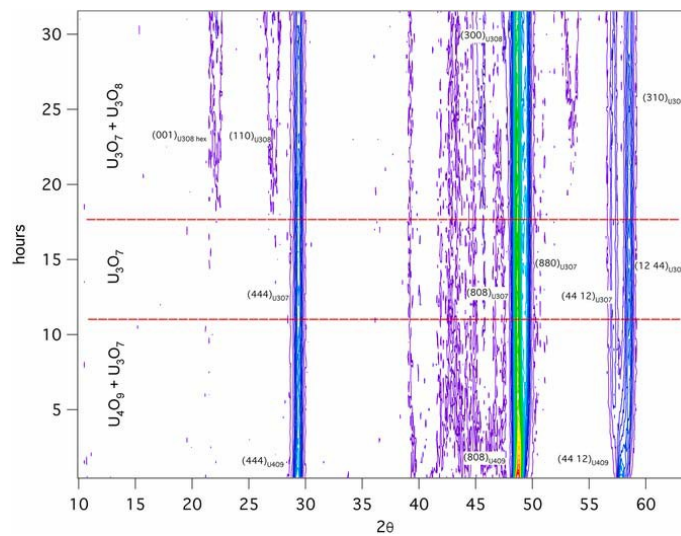

Fig. 15 Kinetics of isothermal oxidation of UO_2 at 480K. Neutron diffraction patterns measured with the diffractometer D2b at ILL, Grenoble. Reproduced with permission from Desgranges, L., Baldinozzi, G., Rousseau, G., Nièpce, J.-C., Calvarin, G., 2009. Inorg. Chem. 48 (16), 7585–7592.

oxygen sublattice of these compounds. Structural and microstructural changes occur in this system and the kinetic laws of these transformations can be determined.[133–135] For example, at 210°C, UO_2 is completely converted into U_3O_7 after 10 h and the U_3O_8 phase characterized by a swelling volume of more than 30% begins to appear after 17 h (**Fig. 15**). The appearance of this phase is detrimental to the mechanical integrity of the fuel rods and a severe problem for waste management.

Detailed knowledge of the three-dimensional structure of solids at the atomic level is a prerequisite for understanding and predicting the properties of materials. Diffraction techniques are able to provide the positions of the atoms (e.g, the Rietveld method for powder diffraction). However, when the solid is not perfectly periodic, the number of coordinates that describes the system increases rapidly (lowering of symmetry, super cells, etc.). Beyond the complexity of the model (the volume of the conventional cell of some of these phases is > 10,000 Å^3) it is also the problem of the interpretation of the model (how to extract the relevant information) and its robustness compared to the very large number of parameters involved its definition; depending on the type of disorder (massively disordered phase, glassy, aperiodic, etc.). These considerations have led to a tentative comparison of the experimental determination of these structures to DFT and Molecular Dynamics predictions.[136–138] Multiple techniques, best adapted to these large systems should be implemented together to improve the description of the important details of these structures (the long-range periodicity, the distribution of first neighbors, local symmetries, ...). Among these techniques, total scattering methods based on the analysis of the pair distribution function (PDF) can provide information on the qualitative and quantitative differences between local structure and long-range order.[133–135]

The use of PDF and Rietveld analysis allows to show that the incorporation of oxygen at intermediate temperatures results in the rapid formation of clusters, sets of oxygen atoms arranged to form a cuboctahedron. These complex defect clusters vary in number (12 in U_4O_9 and 16 in U_3O_7) and have different local symmetries in each phase: almost perfectly regular in the β-U_4O_9 but distorted in α-U_4O_9 and rotated about a fourfold axis in U_3O_7. The structure of U_3O_7 is still under discussion as a recent TEM study[139] suggests that the symmetry previously used can be the result of the averaging of correlated domains. The local structure of the cuboctahedron clusters in the deformed configurations[140,141] foresees the topology of U_3O_8 bonds, a phase characterized by a rearrangement of the crystal planes and that can be described by a mechanism similar to martensitic transition observed in other compounds.[142]

The information on the structure at the atomic scale has been included in a model for the kinetics of oxidation that makes use of two different diffusion coefficients for oxygen in U_4O_9 and U_3O_7 phases. In this model, the appearance of the phase U_3O_8 is a function of the oxygen potential of the ambient atmosphere, but also of the initial stress state of the sample. This model seems to provide a reliable criterion for defining reliable safety conditions for the dry storage of spent fuel[143] that links chemistry and mechanical properties.

2.6 Radiation-Induced Mechanical and Microstructural Effects in Uranium Oxides

During commercial reactor operation, UO_2 undergoes radiation damage for a period of about 5 years. This changes the microstructure and the macroscopic properties. Also, the chemical composition displays a change because of the ongoing production of fission products, α,- and β-decays. This also leads in changes in the chemical and physical properties of the fuel. The radial temperature profile within a pellet and the local radiation flux are responsible for a very heterogeneous system: the resulting properties of the fuel are then not only function of the average burnup, but also of the exact radial position under consideration within the nuclear pellet. Moreover, extremely active fission products continue to produce high radiation fluxes during interim storage of the spent fuel. These effects, then continue to produce changes of the topology of defects and the microstructural properties for very long times. The direct analysis of these changes can be performed at very few installations (as for instance the Merarg test equipment, at Leca-Star facility in CEA Cadarache) because of the radiotoxic and hazardous nature of these fuel elements. Parametric studies on simplified systems are then needed to complement those studies. Volume change is perhaps the most apparent effect occurring during and after irradiation, mostly related to the accumulation of point defects that promote the increase of the cubic lattice parameter. At high burnups, this value exhibits a saturation that marks the appearance of extended features.[144,145] Nevertheless, fission gases produced by fissions are responsible for most of the observed macroscopic swelling of the fuel, even after the saturation of the lattice parameter. Bubble formation and gas diffusion modify the mechanical and thermal properties of the fuel rod are harmed, so their understanding is crucial. During the operation in the reactor, athermal fission-enhanced diffusion processes dominate below 1000°C, and they represent an important mechanism in the rim region of the nuclear fuels. This mechanism is affected by other parameters, as departure from stoichiometry, local chemistry, and particular microstructural features (as for instance microporosity) that can interact with the fission gases.[146–148] In some cases, for particular burnup and temperature conditions, the concentration of gas bubbles seems sufficient to release a burst of fission gases, eventually producing cracks in the fuel pellet.

It is difficult to detail all the changes occurring in the nuclear fuels, but most of the effects already described change their mechanical properties: spent fuels possess a modified microstructure, with particular porosity distributions, anisotropic recrystallization and grain polygonization.[149] An example is the radial change in the elastic modulus of nuclear fuel[150,151]: hardness is found to increase for increasing fuel burnups and the onset of porosity in the rim of the fuel pellets (over a 200 μm thickness from the edge) affects the mechanical properties in this region. Also, in this region, higher neutron fluxes lead to increased resonant neutron capture rates by ^{238}U and to the production of ^{239}Pu. This high burnup structure (HBS) is also locally observed near Pu-rich zones in heterogeneous MOX fuels.[152] The mechanisms responsible for these changes are not clearly understood yet, but they seem to correlate with the polygonization processes. TEM and SEM observations performed[99,153] suggest the initial grains are subdivided rather than recrystallized in the HBS. It is not yet clear whether the HBS has a beneficial effect on the radiation resistance of the nuclear fuel. The high burnup structure that develops in the outermost regions of the nuclear fuel pellets has characteristic morphological features. The determination of the specific mechanical properties of these regions with a very high density of grain boundaries and interfaces should be fostered because they are of

paramount importance for the safety of spent fuel and repository solutions. They represent the spent fuel interface facing the external environment (cladding or the external environment in accident conditions). Engineering these microstructures could eventually help developing accident tolerant fuels.

The remarkable radiation resistance of UO_2 seems not only related to microstructural features. The fluorite structure of UO_2 is particularly chemically flexible to allow broad deviations from stoichiometry and aliovalent cation substitutions without catastrophic consequences. Also, UO_2 does not amorphize under severe ionizing radiations.[81,154] A possible explanation involves the peculiar behavior of polarons in UO_2. These quasiparticles consist of an electronic carrier coupled with the strain field they self-generate. UO_2 presents a high concentration of polarons at high temperature.[155] The thermodynamic properties of UO_2 are strongly modified by polarons and simple models allow reproducing some of the observed anomalies with a good accuracy[156,157] because these models involve higher values of the heat capacity that favorably affects the radiation behavior, predicted for instance by thermal-spike models.

3 Silicon Carbide

3.1 Introduction

Silicon carbide (SiC) is an important material for the nuclear energy applications[158–160] as well as for microelectronics at high temperature.[161] SiC is a ceramic with a high thermal conductivity, low thermal expansion, and exceptional resistance to thermal shocks and corrosion in aggressive environments at high temperatures.[162] For nuclear applications, it shows low neutron capture cross sections and low activation. Characterization of radiation damage at different length scales is a critical issue in many materials, and particularly in the case of SiC owing to the existence of many polytypes. Actually, among the known 200 polytypes, the standard easily available ones are the 3C (cubic β-SiC) and the 4H/6H polytypes (hexagonal α-SiC) corresponding to different stacking of the Si and C atom layers. A vast and complex literature was dedicated to point defect and point-defect cluster studies by different spectroscopies and ab-initio simulations summarized in Ref.[163]. Many studies have shown that amorphization (loss of long-range atomic order) can be achieved in SiC by accumulation of point defects (Frenkel pairs and anti-site defects) and defect-clusters above a threshold irradiation dose (or fluence) upon energetic electron[164] or ion[165] and neutron[166] irradiations.

3.2 Amorphization of SiC by Displacement Damage

RBS/C data have indeed shown that complete amorphization of SiC is achieved in two steps, in agreement with MD simulations[167]: the first step corresponds to defect accumulation (to reach amorphization), and the second one to amorphous domain overlap[168–170] (**Fig. 16**). No direct amorphization is achieved in a single collision cascade produced by a single ion impact in SiC. The amorphization dose is of about 0.3 dpa at room temperature[167] and it increases exponentially above the critical temperature of about 500K, owing to dynamic recovery effects.[171] The precise critical temperature values depend on PKA spectrum and dose rate.[166] Amorphization induces a large swelling of this material due to the decrease of the atomic density with respect to the pristine crystal.[168,169,172,173] The amorphization
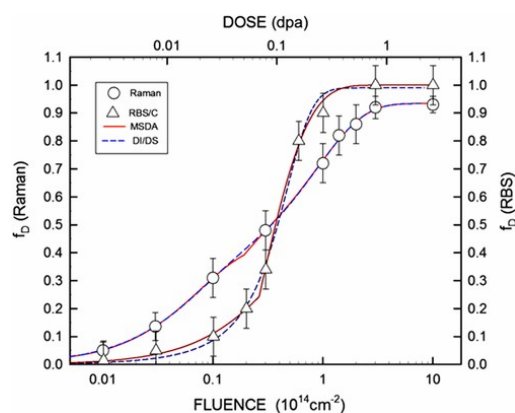

Fig. 16 Damage fraction (f_D) deduced from Raman and RBS/C spectra of 6H-SiC as a function of the 4.0-MeV Au ion fluence with the fits using the Multi Step Damage Accumulation (MSDA, solid line) and the DI/DS (Double Impact-Defect Stimulated, dashed line) models. Reproduced with permission from the publisher (Taylor & Francis Ltd, http://www.tandfonline.com). Miro S., Costantini, J.-M., Huguet-Garcia, J., Thomé, L., 2014. Recrystalization of hexagonal silicon carbide after gold ion irradiation and thermal annealing. Philos. Mag. 94 (34), 3898–3913.

threshold is consistent with the change of volume expansion above a threshold dose near 0.3 dpa.[168,169] The origin of amorphization in relation to point-defect accumulation was widely disputed over the last decade. Different attempts were made to model the amorphization and dynamic annealing processes on the basis of point defect properties.[174–177] Another approach was based on the formation of a chemical disorder inducing a kind of glass transition.[178]

MD simulations have shown that a total volume swelling smaller than 4% occurs for point-defect accumulation, during the first step of damage for low disorder fractions (<10%). Amorphization sets in at a total swelling exceeding 6.5% corresponding to lattice softening in the second step of damage for high disorder fractions (>10%) (**Fig. 17**).[179] Full amorphization, beyond a total swelling of 8%, leads to a large decrease of the Young's modulus and to the collapse of the elastic constants.[19,179–181] The values of E_d of Si and C atoms which are fairly anisotropic for the 3C and 6H polytypes have been subject of a long-standing debate between different authors.[16,181–186] Different spectroscopies were applied to determine these values such as RBS/C[187] or photo-luminescence of the Si vacancy (V_{Si}^-).[188]

Raman spectroscopy is widely used to unambiguously identify the various polytypes of SiC, whereas it is a most difficult task by using XRD.[189] First-order Raman peaks at wavenumbers of 790 cm^{-1} and 970 cm^{-1} correspond to the transverse (TO) and longitudinal (LO) optical phonons at the Brillouin zone (BZ) center (Γ point).[190] Calculations of the phonon dispersion curves for hexagonal polytypes (4H- and 6H-SiC) and cubic polytype (3C-SiC) predict a broad gap between the acoustical TA/LA and optical TO/LO modes from about 600–800 cm^{-1}[190–192] in contrast to results in Si and Ge,[193,194] an effect due to the polar bonding character. Atomic disorder usually induces shifts and broadening of these peaks, due to the loss of long-range periodicity selection rules and distortions of the structural building blocks (coordination polyhedra) associated with a randomization of bond lengths and bond angles.[195] Moreover, the decrease of phonon life time (viz., mean free path) due to lattice disorder and defects may also contribute to inhomogeneous peak broadening.[196]

The progressive loss of long-range order was also witnessed by the vanishing of the narrow Raman peaks associated with phonon modes of the 4H/6H polytypes after heavy ion irradiations[197–199] (**Fig. 18**). This was accompanied by an increase of the backscattering yield in RBS/C experiments on single crystals, corresponding to disorder into the Si sublattice.[168,171] Micro-Raman spectroscopy also allowed assessing the damage of polycrystalline β-SiC samples after high-temperature neutron irradiation.[200] The asymmetry of the TO (near 790 cm^{-1}) and LO (near 970 cm^{-1}) phonon peaks in neutron irradiated β-SiC and 6H-SiC, originally with a symmetric Lorentzian shape, was interpreted by a phonon confinement model within small domains.[199,200] Furthermore, micro-Raman spectroscopy was also used to probe the local damage profile following 20-MeV Au ion implantation in a 6H-SiC crystal that show three distinct damaged zones.[201] Fourier transform infrared (FTIR) spectroscopy data have also shown a progressive intensity decrease and broadening of the TO and LO phonon peaks of 3C-SiC epilayers grown on a Si substrate after 2-MeV Si ion irradiation. This is consistent with former results by Raman spectroscopy and a threshold dose of about 0.3 dpa.[202] Broad bands with Gaussian shapes were recorded at large fluences, when amorphization was reached, in relation to randomization of bond lengths and bond angles in a-SiC.[203]

Ab-initio calculations concluded that the short-range order in the amorphous phase keeps the tetrahedral environment with sp^3 covalent bonding, in the first coordination shell of Si and C atoms.[204] In this case, Si atoms are the nearest-neighbors (NN) of C atoms and reciprocally. Hence, disorder at large scale may be induced by the disorientation of these SiC$_4$/CSi$_4$ tetrahedral building blocks. Raman spectra of the amorphous (a-SiC) phase show the growth of broad side bands assigned to Si–Si and C–C bonds, but also distorted/disordered Si–C vibration modes, which do not exist in the pristine crystalline phase.[198,205,206] This means that a chemical disorder was created upon amorphization, in agreement with extended X-ray absorption fine structure (EXAFS) results[205] that provide evidence of the existence of homopolar NN bonds.[164] This is quite similar to the III-V compounds in which evidence of "wrong bonds" in the first coordination shell was also found in their amorphous phases on the basis of EXAFS experiments.[207,208]

The short-range chemical disorder (given by the growth of the broad C–C and Si–Si homonuclear bands) was correlated to the long-range disorder (given by the vanishing of narrow Si–C phonon peaks) by a three-stage defect accumulation process in 4-MeV Xe and 4-MeV Au ion irradiations of 4H/6H polytypes[198,206] (**Fig. 19**). The first stage (I) is consistent with the above-mentioned first step of point-
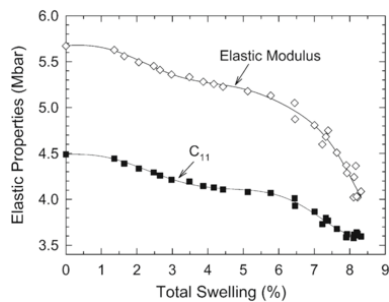

Fig. 17 Elastic modulus and elastic constant (C$_{11}$) of SiC as a function of volume swelling computed by MD simulations. Reproduced with permission from Weber, W.J., Gao, F., 2010. Irradiation-induced defect clustering and amorphization in silicon carbide. J. Mater. Res. 25 (12), 2349–2353.
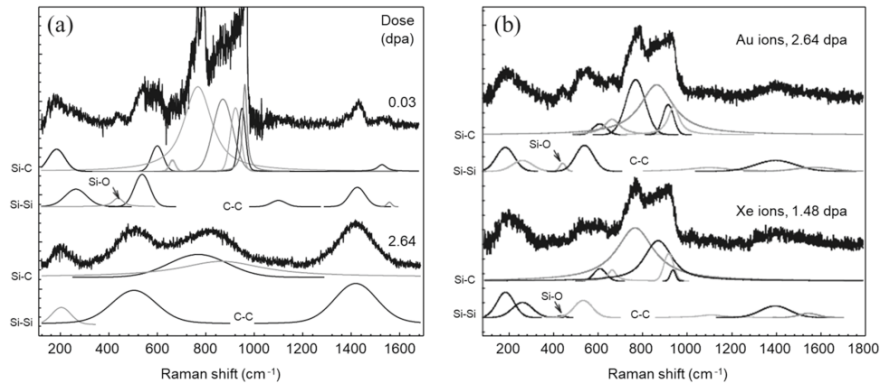
Fig. 18 Raman spectra of 6H-SiC after 4.0-MeV Au ion irradiation at RT for different doses in dpa. The various bands in colors used for fitting are shown below the experimental spectra in black: heteronuclear Si-C bands (blue), homonuclear Si-Si (red) and C-C (purple) bands. Reproduced with permission from Sorieul, S., Costantini, J.-M., Gosmain, L., *et al.*, 2006. J. Phys. Condens. Matter 18 (22), 5235–5251.
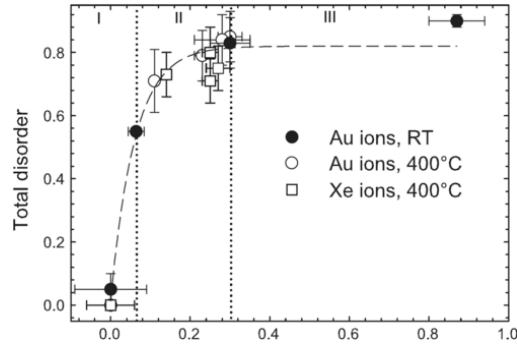

Fig. 19 Total disorder deduced from the vanishing of phonon peaks of 6H-SiC in Raman spectra as a function of the chemical disorder deduced from the growth of the homonuclear Si–Si and C–C bands as a function of dose (see **Fig. 18**) for 4.0-MeV Au and 4.0-MeV Xe ion irradiations at RT and 400°C. The dashed line is a fit with an exponential law. The three stages of accumulation of damage are shown by I, II and III. Reproduced with permission from Sorieul, S., Costantini, J.-M., Gosmain, L., *et al.*, 2006. J. Phys. Condens. Matter 18 (22), 5235–5251.

defect accumulation seen by RBS/C spectrometry. The transition between stage I and stage II to reach amorphization corresponds to a ratio of homonuclear bonds to heteronuclear bonds close to 0.3, in agreement with MD simulations.[178] However, a clear deviation was seen between Raman and RBS/C data,[170] in agreement with literature data on 50-keV Ga ion irradiation in 6H-SiC in the same fluence range.[209] Raman spectroscopy is apparently more sensitive to a lower damage than RBS/C and it gives a clearly larger disordered estimate than RBS/C in the first stage (**Fig. 16**).

Relative Raman intensity (RRI) variations were generally used to follow the irradiation damage in SiC.[198,209–211] This RRI index is based on the decrease of the Raman peak intensities. It reflects the long-range disorder induced in the crystal, even though there is no straightforward relationship between the RRI index and the lattice disorder fraction. The total disorder $(1 - A_{norm})$ was defined calculating the total area A under the principal first-order Raman peaks normalized to the value A_{cryst} of the crystalline material ($A_{norm} = A/A_{cryst}$).[198,206,209] Since the classical selection rules of periodic solids using the lattice-vibration wave vector are broken in a disordered solid,[195,196,212] the folded phonon density-of-states (DOS) at the Γ point involves contributions of vibration mode branches of various symmetry labels of other points of the BZ.[212] Even low-frequency TA/LA modes and IR-active *ungerade* modes may become Raman active due to disorder, as in a-Ge or a-Si for instance: Raman spectra may then reflect the total phonon DOS.[196,212,213] In principle, this

prevents to monitor the decrease of long-range order by the decrease in intensity of a specific phonon peak owing to the overlap of these contributions at a same phonon energy (i.e., same Raman wavenumber).

Even if the appearance of new broad Si–Si and C–C vibrational side bands in the Raman spectra[198,199] is quite puzzling, and not quite completely understood, it is actually consistent with several MD simulations of the short-range order in a-SiC[178,214–216] These side bands could also be associated either to small Si and C clusters formed by radiation-induced segregation like in some metallic alloys,[217] or to a new local order (within the first shell) associated with defect accumulation (like anti-site defects on both sub-lattices).[180] Experimental data (EXELFS and HRTEM) on electron-irradiated SiC showed that no formation of Si or C clusters takes place in the amorphous phase during room-temperature irradiations.[167] On the other hand, such clustering was seen in the case of high-temperature irradiations, where a partial recrystallization of the material has occurred due to in-beam dynamic annealing effects.[218] The Si–Si and C–C correlations in the first coordination shell were derived from the radial distribution functions (RDF) deduced from electron-diffraction data[167,219] and from partial RDF deduced from EXELFS data.[218] These RDF are consistent with ab-initio simulations[203,214,220] and EXAFS analysis[221] of the chemical order with C–C bonds (~1.5 Å) shorter than the Si–C bonds (~1.9 Å) and the Si–Si bonds (~2.3 Å). Attempts to reproduce these side bands was performed by ab-initio simulations.[222] Given some assumptions on point defect formation (carbon anti-site C_{Si} and carbon anti-site complex $V_C C_{Si}$) involving C-C bonds, a Raman-active peak at 630 cm^{-1} is predicted in the phonon DOS. However, the higher wave number modes above 1030 cm^{-1} were not reproduced. A peak at 575 cm^{-1} was associated to $V_C C_{Si}$ in neutron irradiated 6H-SiC.[199]

No specific internal vibration modes of the SiC_4 building blocks can be isolated in covalent SiC, unlike the polyhedra in ionic compounds.[223] The decrease in intensity of the collective vibration modes seen in the Raman spectra of SiC is certainly related in a more complex way to damage accumulation upon irradiation. However, point defects induce localized electronic levels (in stage I), and long-range disorder generates band tails of electronic extended states in the band gap (in stage II).[224] This, in turn, induces an increase of self-absorption of Raman signals for a laser line with photon energy of about 2.3 eV. Indeed, UV–visible absorption spectra showed a clear shrinkage of the optical gap width from about 3 eV to 0.5 eV, and an increase of the Urbach edge with the irradiation dose, until saturation is reached in the amorphous phase.[206,211] Henceforth, self-absorption of the scattered light inside the damaged layer cannot be overlooked: this definitely contributes to the greater sensitivity of Raman spectroscopy to the atomic disorder.

3.3 Mechanical Properties of Irradiated SiC

Knowledge of mechanical property evolutions upon neutron irradiation is a key issue for the nuclear applications.[19,225] Several early studies were dedicated to neutron irradiated SiC ceramics.[18,21,226] An emphasis was placed on the volume swelling and evolution of mechanical properties under neutron irradiation.[227] Nano-indentation measurements on 3C-SiC and 6H-SiC single crystalline samples and hexoloy polycrystalline samples showed that the Young's modulus and hardness are progressively reduced after 4-MeV Xe and 4-MeV Au ion-irradiations above a 15%–20% disorder fraction threshold measured by RBS/C corresponding to the onset of amorphization.[169,181] A strong decrease of Young's modulus of 25% (in 3C-SiC) or 40% (in 6H-SiC) and of hardness of 34% (in 3C-SiC) or 47% (in 6H-SiC) was reached in the amorphous phase compared to the parent crystalline phase, in agreement with the MD simulations.[180,228] Amorphization may also take place during nano-indentation due to dislocation coalescence.[229] Even though the starting polytype has different mechanical properties, the same values are obtained for a-SiC after irradiation. Standard homogenization models were used to calculate the dependence of these data against disorder fraction[169] (Fig. 20). A corresponding volume swelling of about 20% was deduced from step-height measurements,[169] whereas other ion irradiation results found a density of the relaxed amorphous phase smaller than the crystalline phase by 7.4 ± 0.9%.[172] This is in rather good agreement with the value of 11.5 ± 2% deduced from XPS and Electron Energy Loss Spectroscopy (EELS) experiments on ion irradiated SiC.[19,166,173,227] Dynamic annealing effect for high irradiation temperature will ensure that such a loss of mechanical properties will not occur above the critical temperature of about 500K.[165]

3.4 Radiation Damage Recovery

Full recovery and almost complete regrowth of the 6H-SiC crystalline phase was achieved after thermal annealing of the amorphous phase at about 1000°C, as followed by Raman spectroscopy[170] (Fig. 21). Densification starts above temperature near 200°C. A first step of relaxation of the amorphous phase takes place at about 700°C with a rearrangement of the Si–Si and C–C homonuclear bonds.[219,230] Other FTIR spectroscopy data also concluded that a relaxation of the amorphous network of a-SiC occurs between 200°C and 800°C before recrystallization at higher temperature.[231] A different kinetics of recrystallization was found for partially and fully amorphous SiC.[170,232,233] A good agreement was found between Raman spectroscopy data for fully amorphous SiC[170] and FTIR data on a-SiC thin films grown on a Si substrate, yielding an activation energy for recrystallization of about 5 eV.[234,235] Evidence of the formation of graphitic clusters at ~1500°C was also provided by Raman spectroscopy,[230] as in a-SiC thin films deposited on a Si substrate.[236] For a large irradiation dose about 3 dpa, exfoliation of the surface occurs at such high temperatures.[170]

3.5 Effects of Electronic Excitation on Radiation Damage in SiC

Another major issue for nuclear applications is the role of electronic excitations that could be deposited by the fission fragments (FFs). Although direct track formation due to SHI effects has not been observed in SiC up to stopping powers of 34 keV/nm, indirect electronic excitation effects may nevertheless occur.[237] Indeed, ionization-induced annealing of pre-existing defects was found for heavy ion irradiations between about 1 MeV to 20 MeV above a low threshold electronic stopping power.[238] MD simulations were carried out[239] to
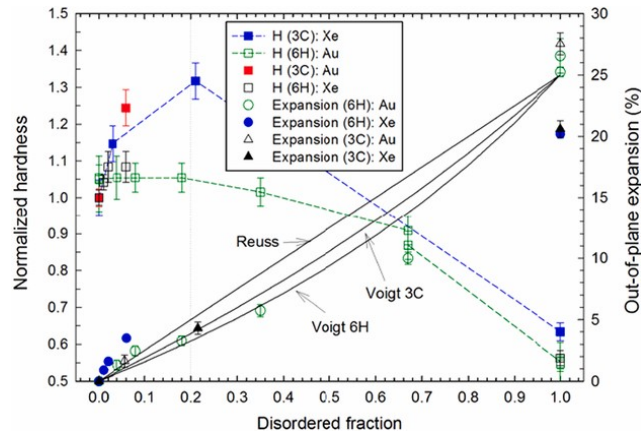
Fig. 20 Normalized hardness and out-of-plane expansion (swelling) of 3C-SiC and 6H-SiC as a function of the disordered fraction deduced from RBS/C data for 4.0-MeV Au and 4.0-MeV Xe ion irradiations at RT. Solid lines are calculations of the expansion with the Reuss and Voigt homogenization models. Dashed lines are guides for the eyes. Reproduced with permission from Costantini, J.-M., Kerbiriou, X., Sauzay, M., Thomé, L., 2012. J. Phys. D Appl. Phys. 45 (46), 465301.
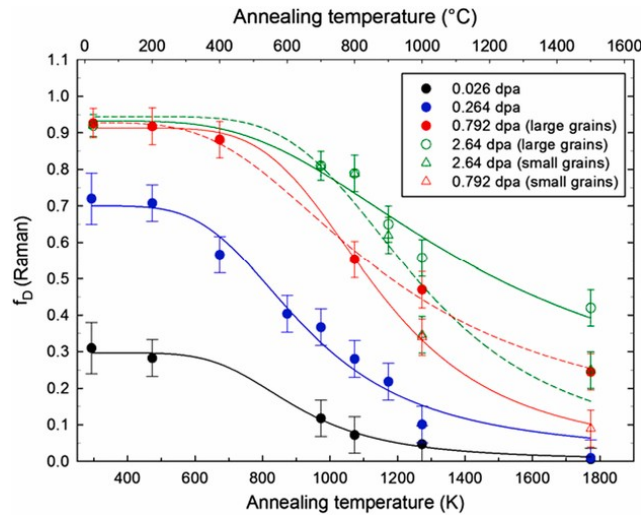

Fig. 21 Damage fraction deduced from Raman spectra of 6H-SiC after 4.0-MeV Au ion irradiation as a function of annealing temperature for various doses in dpa. Reproduced with permission from the publisher (Taylor & Francis Ltd, http://www.tandfonline.com). Miro S., Costantini, J.-M., Huguet-Garcia, J., Thomé, L., 2014. Recrystalization of hexagonal silicon carbide after gold ion irradiation and thermal annealing. Philos. Mag. 94 (34), 3898–3913.

model this kind of recovery induced by electronic excitations that was already observed during the RBS/C experiments with He ions in the MeV range.[240] However, these effects play a minor role in the dynamic recovery process for various irradiation temperatures.[165] The coupled effect of the nuclear stopping power and electronic stopping power was studied for various heavy ion energies from about 5 MeV

to 25 MeV.[241] Defects induced by nuclear collisions can actually be annealed out by in-cascade ionization processes. Enhanced recrystallization by SHIs was found for partially and fully amorphous SiC.[242]

3.6 SiC Nanocrystals and Fibers

Nanocrystalline forms of SiC (nano-engineered) were also investigated to check their radiation resistance with respect to single crystalline 3C-SiC using Si ion irradiation in the MeV energy range.[243–245] No clear-cut conclusions on the radiation resistance were drawn since results depend on the ion energy. The stacking faults and the related strain field were found to play a key role in the radiation resistance of the nanocrystalline material.[244] Moreover, MD simulations have shown that the grain size is a key parameter for the defect production rate.[246]

Finally, the behavior of SiC fibers and SiC/SiC composites under ion and neutron irradiation was studied for use as structural materials in high-temperature gas-cooled reactors.[160] Irradiation creep and fracture toughness are known to be major issues for maintaining integrity of nuclear fuel cladding in a wide range of temperature, including the case of loss of coolant accident conditions (LOCA). For this purpose, relevant neutron irradiations of Hi-Nicalon Type S silicon carbide composites were carried out.[247] Amorphization of third-generation 3C-SiC fibers (Hi-Nicalon type S and Tyranno SA3) and 6H-SiC single crystals were studied after 4-MeV Au ion irradiation experiments at room temperature: kinetics are similar despite the difference in polytypes.[248] A similar cracking and exfoliation process was found after annealing of both kinds of amorphized materials up to 1000°C: the activation energy of the cracking process is close to that for recrystallization.[248] In-situ environmental scanning electron microscopy (E-SEM) and TEM observations of both kinds of materials show that the recrystallization process is the stress source of cracking and exfoliation.[249] Moreover, an irradiation-induced creep was observed by in-situ mechanical tests on Tyranno SA3 fibers at 1000°C and under 300 MPa upon 92-MeV Xe ion irradiation as a function of flux[250] (**Fig. 22**). These samples displayed negligible increase of thermal creep and no amorphization.[251]

4 Normal Spinel Structure Oxides

4.1 Introduction

The normal spinel structure oxide, AB_2O_4, belongs to Fd-$3m$ in Wyckoff notation, in which oxygen ions form fcc structure, and A and B cations occupy the tetrahedral and octahedral sites, respectively.[45,252] The occupation probability of the (ideal) normal spinel structure is 1/8 for tetrahedral sites (A ions) and 1/2 for the octahedral sites (B ions). The remaining sites of tetrahedral and octahedral sites are empty interstitial sites or structural vacancies (**Fig. 23**). Magnesium aluminate spinel, $MgAl_2O_4$, is a normal spinel structure oxide, and it has been recognized as an excellent radiation resistant ceramic, especially to void swelling. $MgAl_2O_4$ is, therefore, expected for IMF,[253] or Rock-like fuel,[254] and functional materials for fusion devises, such as a diagnostic probe and a high frequency window for plasma heating.[255,256] Additionally, this material has been investigated as a model material to understand the radiation resistant mechanism of ceramics. Explanation for the radiation resistance and microstructure stability of $MgAl_2O_4$ was reviewed in the first edition of the Comprehensive Nuclear Materials, with a comparison of α-Al_2O_3 from a view point of the difference in the stacking layer of {111} planes,[257] and in others.[258,259] In this section, we will review the mechanism of the microstructure stability, dimensional and mechanical properties of $MgAl_2O_4$, and will introduce an attempt to understand the microstructure stability of normal structure spinel oxides from the rearrangement of correlated nanoscale domains.
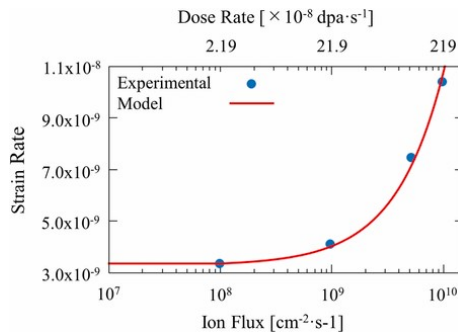

Fig. 22 In-situ measurement of Tyranno SA3 Strain rate versus flux and dose rate upon 92-MeV Xe[23+] irradiation at 1000°C and 300 MPa. Produced from unpublished work of Huguet-Garcia, J., Jankoviak, A., Miro, S., *et al.*, 2015. EPJ Nucl. Sci. Technol. 1, 8.
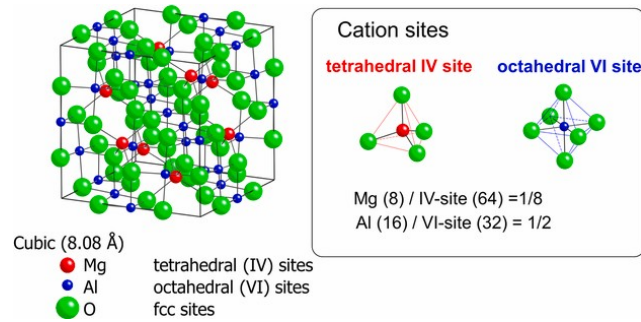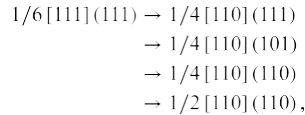
Fig. 23 Crystal structure of ideal MgAl$_2$O$_4$ spinel (a), the octahedral (IV) and tetrahedral (VI) sites in spinel structure are shown in (b) and (c), respectively. Occupation for octahedral and tetrahedral sits in an ideal spinel is 1/2 and 1/8, respectively.

4.2   Mechanism of Radiation Resistance of MgAl$_2$O$_4$

Based on the crystal structure and other characteristic features, the radiation resistance of MgAl$_2$O$_4$ is explained by a few factors. One is the large nuclei of stable interstitial-type dislocation loops: the nuclei is supposed to be anti-Schottky septets, or a composition of MgAl$_2$O$_4$, to keep the charge neutrality.[260] The nature of interstitial-type dislocation loops at rather low temperature has been proposed to follow the progressive growth with neutron irradiation by changing their Burgers vector and the habit planes,

$$1/6\,[111]\,(111) \rightarrow 1/4\,[110]\,(111)$$
$$\rightarrow 1/4\,[110]\,(101)$$
$$\rightarrow 1/4\,[110]\,(110)$$
$$\rightarrow 1/2\,[110]\,(110),$$

which indicates that the nature of interstitial dislocation loops changes from the nonstoichiometric loops without compensating the charge neutrality to the perfect type dislocation loops.[261,262] A second mechanism relates the cation exchange or point defect recombination between the octahedral and tetrahedral sites through the empty interstitial sites under irradiation.[263] A neutron diffraction study revealed the site exchange between Al ions at octahedral sites and Mg ions at tetrahedral sites. This leads to the exceptionally low number of interstitials of only 0.002%–0.9% retained in the form of dislocation loops under neutron irradiation in MgAl$_2$O$_4$.[261,262] Electron irradiation with a high voltage electron microscope, with which only isolated Frenkel defects are induced, showed that dislocation loops were hardly nucleated, due to the high recombination rate of point defects.[260]

Another factor to be considered is the sensitivity to electronic excitation. Synergistic irradiation of high intensity electronic excitation (or high electronic stopping power) with displacement damage (nuclear stopping power) was found to retard the nucleation of interstitial-type dislocation loops.[11,264,265] A parameter of number of electron-hole pairs/dpa ratio well explains the retardation of dislocation loops.[264] The values of electron-hole pairs/dpa ratio where no dislocation loops is formed is approximately 30 for MgAl$_2$O$_4$, whereas MgO and α-Al$_2$O$_3$ showed significantly higher values of 10^3 and 10^4, respectively.[264] Namely, MgAl$_2$O$_4$ is sensitive to electronic excitation to retard the nucleation of interstitial-type dislocation loops. This electronic excitation effects were discussed in terms of the enhancement of point defect migration due to ionizing radiation (ionization-induced diffusion),[264,266] and the change in the charge state of point defects which influence the migration energy of point defects.[267] The excitation sensitivity also relates the stability of non-stochiometric dislocation loops with the nature of 1/6 {111}<111> loops, which disappear under electron irradiation for a transferred kinetic energy lower than the threshold displacement energy (E_d).[260] An empirical MD simulation study reported the recommended values of E_d in MgAl$_2$O$_4$ for O, Al and Mg to be 60 eV, 30 eV and 30 eV, respectively.[268] It was also reported that E_d values depend on crystallographic orientation: for example, those values for O ranged from 27.5 eV (<100> direction) to 105.8 eV (<110> direction).[269] UV–visible optical absorption data of F centers (oxygen vacancies) for electron-irradiated MgAl$_2$O$_4$ have shown that the effective E_d of O is large (> 130 eV) at room temperature.[270,271]

Fig. 24 shows that small dislocation loops formed by 3 keV Ar ions were eliminated with 200 keV electron irradiation.[10] The transferred energy from 200 keV electrons are below the values of E_d reported by the literature.[268–271] It is seen that the density and size of dislocation loops decrease with electron irradiation (an example is shown by "A" and "B" in **Fig. 24**), although some dislocation loops grow under electronic excitation (an example is indicated by "C" in **Fig. 24**). Through an analysis of the change in the density and size of dislocation loops, the elimination of dislocation loops in MgAl$_2$O$_4$ was attributed to electronic excitation-induced dissociation of non-
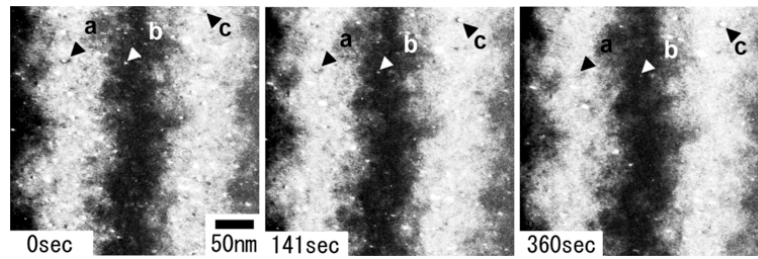
Fig. 24 A sequence of weak-beam dark-field (WBDF) images of $MgAl_2O_4$ irradiated with 200 keV electrons at 300K for (a) 0 s, (b) 141 s and (c) 360 s with an electron flux of 6.1×10^{18} m^{-2} s^{-1}. Interstitial-type dislocation loops, appeared as white or Black dot contrast, were introduced before electron irradiation with 3 keV Ar$^+$ ions at the top and bottom surface regions of wedge-shaped specimens. The diffraction condition is (g, 5 g) with a diffraction-vector (g-vector) of g = 220. Dislocation loops are seen either to disappear (an example is indicated by "A"), shrink (indicated by "B") or grow (indicated by "C"). Reproduced with permission from Yasuda, K., Yamamoto, T., Seki, S., Shiiyama, K., Matsumura, S., 2008. Nucl. Instrum. Method B 266 (12–13), 2834–2841.

stoichiometric loops into isolated interstitials without compensating the charge neutrality. The enhanced growth of dislocation loops in $MgAl_2O_4$ was also observed in ion-irradiated $MgAl_2O_4$,[264] which was discussed due to the absorption of interstitials generated by the dissociation of interstitial-type dislocation loops.[10,272] Ionization-induced diffusion is also considered to affect the diffusion process of generated point defects through the dissociation of loops.[10]

4.3 Microstructure and Dimensional Stability of $MgAl_2O_4$ With Different Radiations and Dose

The exceptional resistance to void swelling of $MgAl_2O_4$ was well explained by a microstructure evolution map under fast neutron irradiation (**Fig. 25**).[273] **Fig. 25** shows the characters of dislocation loops and the critical dose for the void or cavity formation in $MgAl_2O_4$ with a comparison of α-Al_2O_3 as functions of irradiation temperature and neutron fluence damage level.[261,262,274–276] Interstitial-type dislocation loops are formed at relatively low temperature (500–600K) and dose (10^{-2}–10^{-1} dpa) for both materials. It is clearly shown in the map that the threshold fluence or dpa for void or cavity formation in $MgAl_2O_4$, which is approximately 100 dpa at 1000K, is about two orders of magnitude higher than α-Al_2O_3. Microstructure observations by TEM revealed that a network of large stacking faults (larger than 1 µm) covered the $MgAl_2O_4$ specimens for irradiation conditions of 1023K and 56 dpa.[262] Voids or cavities were observed at 137 and 217 dpa preferentially only at the vicinity of stacking faults, but not in the matrix.**Fig. 26** shows examples of the networks of stacking faults observed by weak-beam dark-field (WBDF) TEM technique and cavities by BF TEM technique taken at an under-focus condition (b).[262,277] This relatively low level of visible defect cluster accumulation is attributed to the high recombination rate of interstitials with structural vacancies during neutron irradiation.

It is noted that $MgAl_2O_4$ undergoes to a transition to the amorphous state if this material is irradiated with energetic ions to a high fluence at relatively low temperatures. This is a noticeable difference from fluorite-type oxides, such as YSZ, UO_2, CeO_2, which hardly undergo to amorphous state as described in**Section 2**. Yu et al.[278] have found the amorphization of $MgAl_2O_4$ with 400 keV Xe ion irradiation at 100K to a dose of 25 dpa, as shown in a TEM image and the corresponding selective area electron diffractions (**Fig. 27**). Importantly, there is an argument that the amorphous state may be induced due to a chemical effect of implanted ions, since the range of several hundred keV ions overlaps with the displacement damage region. However, the amorphization of $MgAl_2O_4$ was also observed with 1.5 MeV Xe ions after a dose of 35 dpa at 30K, with which the distribution of displacement damage and implanted ions are well separated. Further work is needed to clarify the chemical effect of implanted ions on the amorphization of spinel structure oxides.[279,280] The microstructure evolution of $MgAl_2O_4$ was investigated extensively for irradiation with heavy ions from several hundred keV to a few MeV, which mainly induce displacement cascades, by means of XRD analysis,[281–283] electron diffraction and TEM analysis,[284] electron channeling X-ray analysis (HARECXS: High Angular Resolution Electron Channeling X-ray Spectroscopy) in TEM,[285,286] and RBS/ C.[278,287] Those investigations have found that $MgAl_2O_4$ follows the progressive microstructure change with increasing irradiation fluence as follows: (1) exchange of cations (Al and Mg ions) between octahedral and tetrahedral sites, (2) preferential occupation of cations at octahedral sites to form the defective rock-salt structure. There is also an approach to interpret the evolution of radiation-induced nano scale microstructure with the short- and long-range order analysis, which will be described in the nextSection (4.4) and (3) $MgAl_2O_4$ finally undergoes a transition to the amorphous state. Step by step observations by MD simulations under continuous introduction of Frenkel defects reproduced the microstructure evolution as observed by experiments.[288–290] Namely, cations were found to recombine with structural vacancies by exchanging their sites, and preferentially occupy the octahedral sites. However, no evidence of the transition to amorphous state was observed in those simulation studies.[288,289] The volume expansion of amorphous state $MgAl_2O_4$ was evaluated to be 30%–35% by a MD simulation and step height measurements of the surface of $MgAl_2O_4$ specimens irradiated with SHIs.[291,292] A
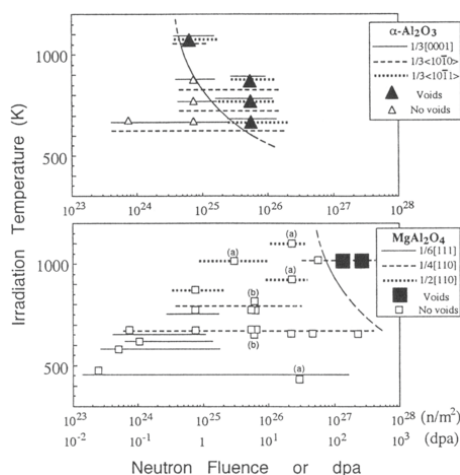
Fig. 25 A map showing the character of interstitial-type dislocation loops and the critical dose for voids or cavity formation in $MgAl_2O_4$ and α-Al_2O_3 as functions of neutron fluence and irradiation temperature. Data are originally from Clinard, Parker, Youngman, Kinoshita, Fukumoto. Values of dpa was estimated from an assumption that a neutron fluence of 10^{21} cm^{-2} (E > 0.1 MeV) is equivalent to 1 dpa. Reproduced with permission from Yamamoto, S., de Kock, L., Belyakov, V., *et al.*, 1998. Irradiation tests on ITER diagnostic components. In: Stott, P.E., Gorini, G., Prandoni, P., Sindoni, E., et al. (Eds.), Diagnostics for Experimental Thermonuclear Fusion Reactors, vol. 2. Boston, MA: Springer US, pp. 269–278. Shikama, T., Yasuda, K., Yamamoto, S., *et al.*, 1999. J. Nucl. Mater. 271–272, 560–568. Sickafus, K.E., 2012. Comprehensive Nuclear Materials. Spain: Elsevier, pp. 123–139. Benyagoub, A., Audren, A., Thomé, L., Garrido, F., 2006. Appl. Phys. Lett. 89 (24), 241914. Zhang, Y., Xue, H., Zarkadoula, E., *et al.*, 2017. Curr. Opin. Solid State Mater. Sci 21 (6), 285–298. Ewing, R., Lucas, G., Williams, J., Zinkle, S. J. (Eds.), 2012. Microstructural Processes in Irradiated Materials, vol. 540. Pittsburgh, PA: Materials Research Society, pp. 35–40.
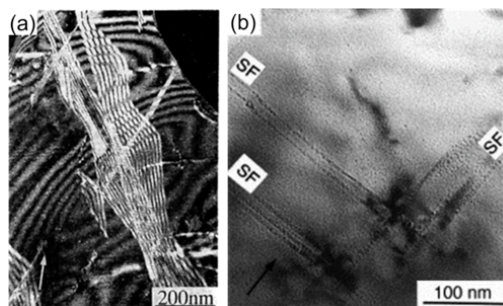

Fig. 26 TEM images of $MgAl_2O_4$ irradiated at 1023K with neutrons to a fluence of 2.17×10^{27} m^{-2}, corresponding to 217 dpa; (a) WBDF TEM image showing networks of stacking faults, taken with a diffraction vector of $g = 113$ (indicated by an arrow). (b) BF TEM image showing voids preferentially at and near the stacking faults, taken with an under-focus condition. Adopted with permission from Fukumoto, K., Kinoshita, C., Garner, F.A., 1995. J. Nucl. Sci. Technol. 32 (8), 773–778. Yasuda, K., Kinoshita, C., Fukuda, K., Garner, F.A., 2000. J. Nucl. Mater. 283–287, 937–941.

recent investigation explains the amorphization resistance of $MgAl_2O_4$ to be directly correlated with the exchange energy of Mg and Al cations or the disordered energy.[293]

Defect accumulation process was also investigated under SHI irradiation. TEM and RBS/C techniques detected the formation of continuous ion tracks and lattice disorder in $MgAl_2O_4$.[292,294–297] TEM observations showed that single SHI induces an ion track in $MgAl_2O_4$ with a core size of 2–3 nm in diameter. The spinel structure is maintained at the core region of the ion tracks although the
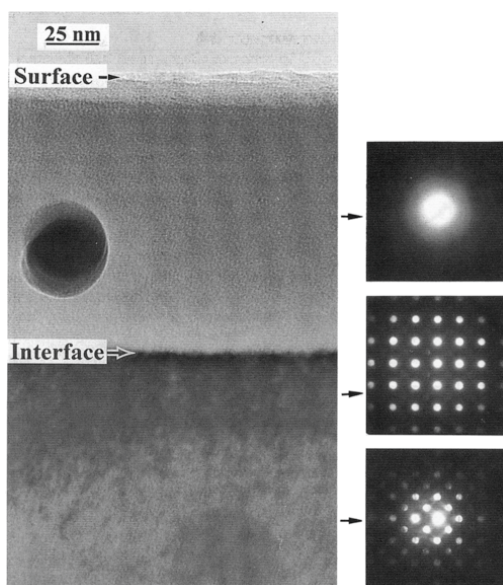
Fig. 27 Cross sectional electron micrograph and microdiffraction pattern of $MgAl_2O_4$ from the (001) direction irradiated with 400 keV Xe ions and 100K to a dose of 1×10^{16} cm^{-2}, corresponding to 25 dpa at the peak depth of displacement damage. The micrograph shows a uniform amorphous layer and corresponding hallow pattern of electron diffraction at the surface layer (130 nm thickness), a defective layer with dark contrast below the interface between the amorphous and crystalline region (40 nm width) and the substrate. The electron diffraction pattern of the defective layer shows the diminish of (220) reflection spots, which indicate the transition to the defective rock-salt structure. Reproduced with permission from the publisher (Taylor & Francis Ltd, http://www.tandfonline.com). Yu, N., Sickafus, K. E., Nastasi, M., 1994. First observation of amorphization in single-crystal $MgAL_2O_4$ spinel. Philos. Mag. Lett. 70 (4), 235–240.

atomic density was decreased, as it was confirmed by Fresnel contrast in BFTEM and HRTEM images.[295–298] These features of ion tracks are same with those observed in fluorite-type oxides, such as CeO_2, YSZ and UO_2 (1.05.2). HAREXCS analysis revealed that single SHI induces random cation configuration of 12.8 nm and 9.6 nm in diameter for Al and Mg ions, respectively,[295] which is significantly larger than defective core region size (2−3 nm in diameter).**Fig. 28** is an example of HRTEM images irradiated with 350 MeV Au ions taken with different size of objective apertures.[296] It reveals that spinel structure is maintained at the core region of a track (c,d), whereas the core region of another ion track (e,f) shows the lattice fringe of defective rock-salt structure, indicating the preferential occupation of cations at octahedral sites. The cation disordering to a random configuration and the transition to rock-salt structure was also observed by HARECXS[295,297,298] and EXAFS analyzes.[299] The progress of microstructure with ion fluence showed the same trend with MeV order heavy ions, although the energy loss between SHI (mainly with electronic stopping) and MeV-ion (large contribution of nuclear stopping) are different. Amorphization by single SHI has not been reported in $MgAl_2O_4$ up to electronic stopping values of ~40 keV/nm. However, significant overlap of electronic excitation damage was found to induce amorphization with 72-MeV I ions at a fluence of 1×10^{16} cm^{-2}.[292] Aruga et al.[300] showed that polycrystalline α-Al_2O_3 was amorphized at room temperature with 85-MeV I ions at a fluence of 2.8×10^{14} cm^{-2}. The threshold fluence for amorphization is about two order magnitude higher for $MgAl_2O_4$ than α-Al_2O_3, which showed again the excellent radiation resistance and dimensional stability of $MgAl_2O_4$.

4.4 Structural Analysis on the Stability of Nanostructured Spinel Oxides

In this section, the current understanding is summarized for the stability of normal spinel structure oxides from an analysis based on short and long range order. The example discussed below is in particular related to the highly ordered normal spinel $ZnAl_2O_4$,[283] but similar considerations also apply to $MgCr_2O_4$ and $MgAl_2O_4$ normal spinel structures that generally exhibit a lesser degree of order in annealed pristine samples. The partitioning of cations between octahedral and tetrahedral sites is temperature dependent, with cations ordering onto preferred sites at low temperatures in the ideal normal spinel. Not limited to $MgAl_2O_4$, oxides with normal spinel structure were the object of intensive studies to assess their structural behavior before and after irradiation[280,301,302] and to evaluate their radiation resistance. As
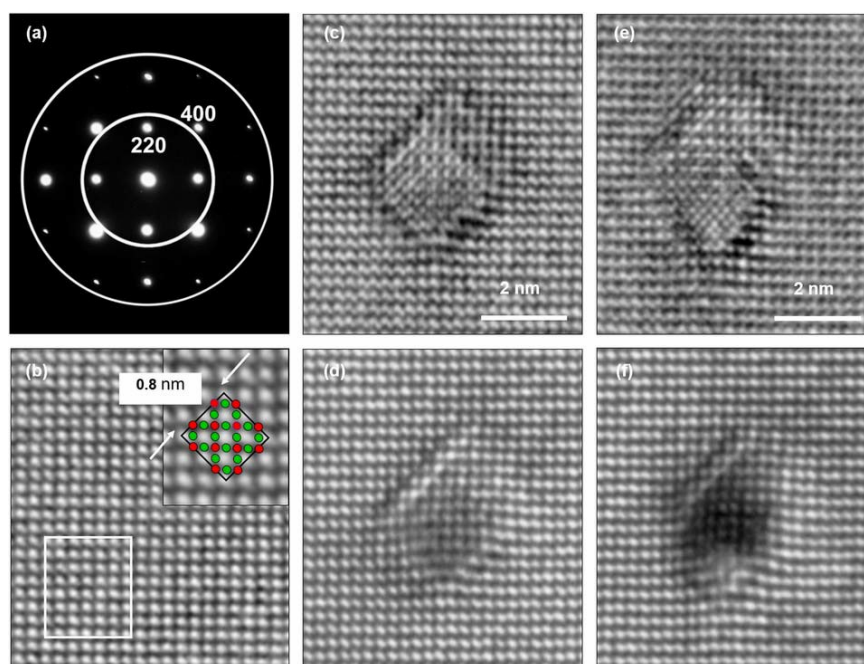
Fig. 28 HRTEM images of $MgAl_2O_4$ irradiated with 350 MeV Au ions to a fluence of 5×10^{11} cm^{-2}. The diffraction pattern for the micrographs, corresponding to a <001> pattern, is shown in (a) with two sizes of objective apertures used for taking micrographs. (b) is for an image from undamaged region with the corresponding projective image of spinel unit cell. Images of (c)–(f) are taken from two ion track regions with larger and smaller objective apertures shown in (a): (c) region I with the larger aperture and (d) the same region but with smaller aperture, (e) region II with the larger aperture and (f) the same region but with the smaller aperture. The core region of ion track (e,f), around 2 nm in size, is discussed to be a defective rock-salt structure. Reproduced with permission from Yasuda, K., Yamamoto, T., Shimada, M., *et al.*, 2006. Nucl. Instrum. Method B 250 (1–2), 238–244.

described in the previous section, in normal spinel structures, the typical diffraction patterns can be indexed in *Fd*-3*m* space group before irradiation and, after irradiation, in a rocksalt-like *Fm*-3*m* space group with a lattice parameter that is halved from the initial value. On the other hand, the number of modes observed in a Raman spectroscopy experiment before and after irradiation is always the same,[283] suggesting the structure at a more local scale (over a few nanometers) is largely unchanged, consisting of the same building blocks (i.e., tetrahedral and octahedral sites). How is it possible to maintain the short-range order in the spinel structure and at the same time explain the change of the long-range symmetry of the diffraction pattern?

Diffraction techniques are very powerful tools to study the crystalline structure and the microstructure. However, Bragg reflections can also spring from materials that are not fully ordered nor homogeneous. Collision cascades produced during low energy irradiation or ion tracks in swift heavy ion irradiations produce severe perturbations of the structure over a few nanometers. After the initial stages of the irradiation, the system generally responds by annealing most of the defects and leaving much smaller concentrations of stable defects. This happens via a reconstruction of the structure, and it happens sometimes that the rapid quenching of those perturbed regions causes their quenching into configurations that do not stack properly in the surrounding pristine crystal. Point defect structures predominate in most non-stoichiometric oxides, but they are not so frequent in stoichiometric oxides like spinel structures. In many oxides, in particular those involving cation bonded in octahedral environments, another mechanism is frequently available leading to extended defects.[303]

In several of these structures, for instance following a reduction reaction, the frequent formation of planar defects known as shear planes is detected.[304] The essential feature of shear planes (**Fig. 29**) is that cation-cation distances can be irregular compared to those of the perfect crystal.[304] The formation of shear planes is therefore typically counteracted by increased cation-cation repulsions of eventual short cation-cation distances. Thus, the creation of those extended metastable defects can rely on the capacity of the structure to accept the relaxation of the cation positions. In the case of spinel, the main structural change concerns the modification of the rutile-like octahedral ribbons: in correspondence of the shear plane, the terminal octahedra of two ribbons become corner-sharing instead of displaying the
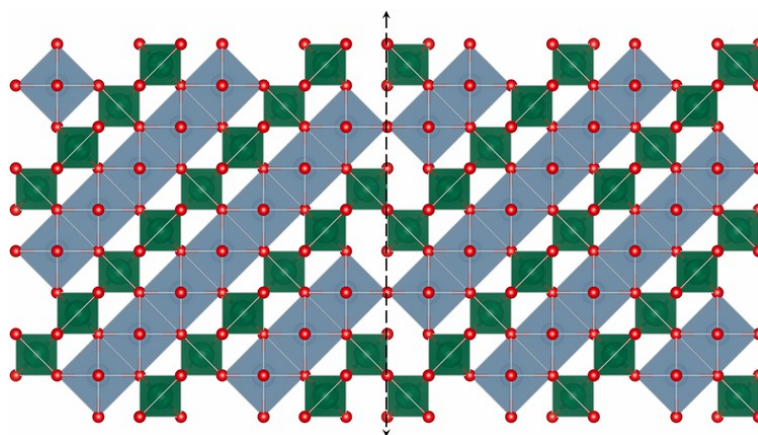
Fig. 29 Example of shear plane between two perfect crystallographic layers of the spinel structure. Green polyhedral are AO_4 tetrahedra, blue ones are BO_6 octahedra. This planar defect displayed in the figure (dashed black line) is actually a plane normal to the pictured layer, but this is not a strict requirement. In the more general case the separation between two nanoscale regions can simply display fuzzy contours.

usual edge-sharing configuration. In this particular process, no unfavorable short interatomic distances between the cations are produced. The possibility of significant densities of shear planes can affect the mechanical properties of the systems as ground state elastic properties are impacted by those modified configurations. The main effect of the shear plane is that the register of the positions of the empty sites, A, and B cations in spinel is messed-up and in the long-range periodicity that is probed by diffraction, while the structure is basically unaffected within a single-variant nanoscale region. Radiation damage in spinel structures can be modeled according to this concept.

The approach consists in considering the nanoscale regions as ordered variants inserted in a host crystal[305] that is the configuration average of all the possible domains (seen as properly dephased replicas of a variant). Sharp Bragg intensities can be observed in correspondence of the reciprocal lattice points of the host crystal, while diffuse scattering occurs from the correlated differences between each domain structure and the average host crystal structure. This diffuse scattering shows up in particular at the reciprocal superlattice spots corresponding to the crystal describing the actual local structure. In the case of spinel, the average symmetry is $Fm\text{-}3m$ with a halved lattice parameter. Diffuse scattering is then observed at the spots of the original $Fd\text{-}3m$ lattice that do not overlap with the average $Fm\text{-}3m$ spots, e.g., (2h,2k,2l) with h, k, and l respecting the $Fd\text{-}3m$ selection rules.

Group theory analysis provides a straightforward way to derive these rules, as the number of ordered variants is simply the number of equivalent classes of $Fd\text{-}3m$ in $Fm\text{-}3m$ (i.e., 8 variants). Since the two groups have the same point symmetry, the 8 cosets are of the type $\{E|t_i\}\otimes G$ where G is the standard set of symmetry operations of $Fd\text{-}3m$ and t_i is one of the 32 vectors belonging to the quotient group of the two translations groups (The eight operator representatives of each coset, using Seitz notation, are (E | 0 0 0), (E | 0 1/4 1/4), (E | 0 0 1/2), (E | 1/4 1/2 1/4), (E | 0 1/4 3/4), (E | 1/4 1/2 3/4), (E | 3/4 1/2 3/4), and (E | 3/4 3/4 0)).

To provide a numerical assessment of this analysis, Monte Carlo simulations can be performed where small regions corresponding to each one of these variants are randomly produced in a large crystal. A crystal consisting of a cube of 50 nm side was simulated. The results in **Fig. 30** were generated displacing randomly chosen small blocks of perfect spinel structure. Their chosen size (5 nm) is not relevant for the demonstration, but it is somewhat representative of the characteristic dimension of the region affected by the displacement cascade and of the same order as the diameter of ion tracks in a swift heavy ion irradiation experiment. The atoms within those nanoscale regions were displaced from their initial positions using the set of vectors t_i already discussed. The inner structure of those blocks is still a perfect spinel structure. At 1 dpa the Bragg intensities of the reflections not compatible with the $Fm\text{-}3m$ space group are lost, while those compatible with the group are almost unaffected. The diffuse scattering is the only remaining signature of the spinel structure and it affects all reflections allowed in the $Fd\text{-}3m$ space group. Therefore, this model explains both the Raman spectroscopy observations and diffraction experiments, suggesting that the normal spinel structure is indeed radiation resistant as the local structure is maintained and the observed long-range change of symmetry is an effect of coherent scattering between correlated domains.

4.5 Mechanical Properties of MgAl$_2$O$_4$, α-Al$_2$O$_3$ and AlN

Mechanical properties investigations on MgAl$_2$O$_4$ are also limited as described in **Section 1**, especially for neutron irradiation.[18,20,306–309] Comprehensive work was performed by KfK group and colleagues[308–310] for sapphire, different grades of sintered α-Al$_2$O$_3$, sintered MgAl$_2$O$_4$, SiC and AlN formed by HIP process for irradiations with neutrons in the order of 10^{25} to 10^{26} n/m^2. A clear and simple
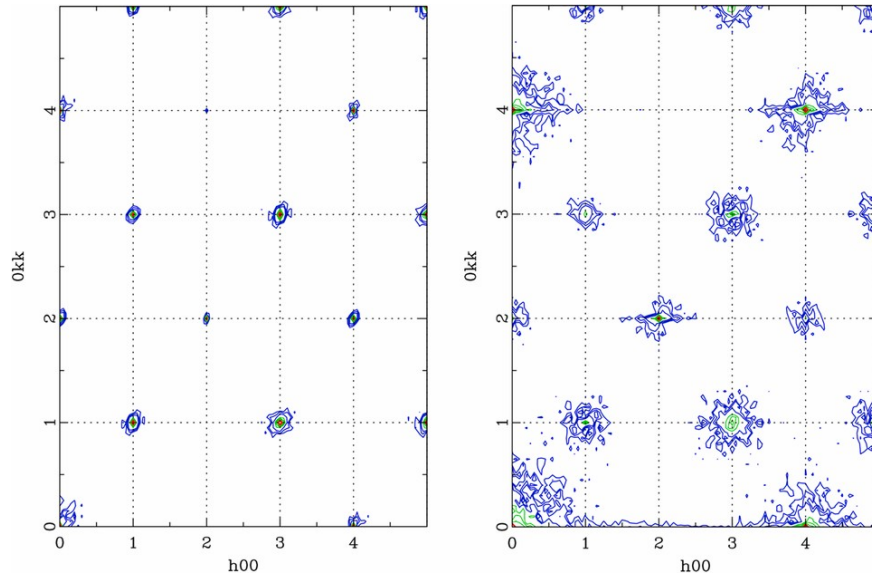
Fig. 30 Monte Carlo simulation of the spinel structure. Left panel, [0-11] zone axis section of the Fourier transform of the pristine structure. Right panel same section for the 1 dpa. structure obtained according to the reconstructive model described in this section. The blue and green contours show the diffuse scattering that increases and broadens for all reflections; red contours are used for the Bragg intensities. Note for instance the total loss of the Bragg component in (111), (311) and (422) reflections and the fact the Bragg intensity remains strong in (222), (400), (044), and (444).

relationship was found between the volume increase and the reduction of Young's modulus (**Fig. 31**).[308] The data sets of both values were within the band formulated with the Young's modulus and the porosity. The decrease in Young's modulus is attributed to the formation of vacancies and/or voids induced by the irradiation. The exception of AlN-HIP data (**Fig. 31**) was interpreted due to the presence of impurity oxygen ions which may degrade grain boundaries or cause micro-crack formation. The decrease in the bending strength was also summarized by the same group for neutron irradiation at temperatures of 373K and 673–873K (**Fig. 32**).[308,309] Bending strength was decreased by neutron irradiation for α-Al_2O_3, SiC and AlN at 373K for a fluence of 2×10^{21} cm^{-2}. This degradation was assigned to the point defect accumulation, because thermally activated diffusion is hardly expected for those ceramics at relatively low temperature of 373K. However, $MgAl_2O_4$ did not show decreases of bending strength at the same irradiation condition, which is contributed to the higher recombination rates of point defects to retard the defect accumulation and aggregation.

As described in **Section 1**, nano-indentation technique has been utilized to measure mechanical properties of the surface region of ion-irradiated $MgAl_2O_4$.[150,311,312] Izumi *et al.* reported the change in hardness on the surface region of $MgAl_2O_4$ and α-Al_2O_3 irradiated with 100 keV He ions at temperatures between 300 and 870K.[312] **Fig. 33** compares the change in apparent hardness (H) as a function of ion fluence, where H is defined as $H = CP_{max}/h_{max}^2$, with P_{max} and h_{max} are maximum load and indentation depth, respectively, and C is the geometrical constant. From the analysis of continuous loading and unloading curves and corresponding TEM observations, the increase and decrease (recovery) of hardness in α-Al_2O_3 observed at fluences less than 10^{16} cm^{-2} were discussed due to the elastic hardening due to the point defects accumulation and their aggregations, respectively. The hardening at fluence higher than 10^{16} cm^{-2} was, on the other hand, attributed to the plastic hardening caused by small dislocation loops. $MgAl_2O_4$ showed the gradual increase in hardness with fluence to reveal again the superior recombination of point defects, resulting in the stability of the mechanical properties. Heavy ion irradiation (150 keV Ar ions) in $MgAl_2O_4$ also showed the increase in hardness at low fluence (in the order of 10^{15} cm^{-2}) followed by the partial decrease in hardness at higher fluence.[313,314]

5 Conclusions

Radiation damage in fluorites, normal spinel structures, and in the semiconductor material SiC allows to probe different facets of the relation existing between chemical bonds, microstructures, and structural complexity. Ion irradiation sometimes acts at the atomic scale to
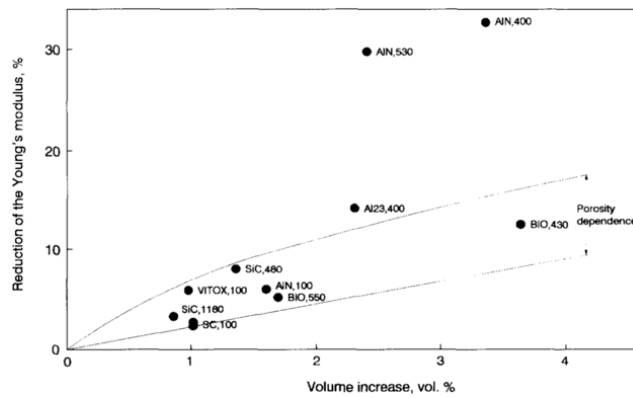
Fig. 31 Correlation between the reduction of Young's modulus and volumetric swelling for neutron irradiated α-Al₂O₃, SiC and AlN. The numbers described in the data points represent the irradiation temperature with a unit of °C. Detail information for the specimens were described in a Ref. Sickafus, K.E., Yu, N., Nastasi, M.J., 2002. Nucl. Mater. 304 (2–3), 237–241. Reproduced with permission from Dienst, W., 1994. J. Nucl. Mater. 211 (3), 186–193.
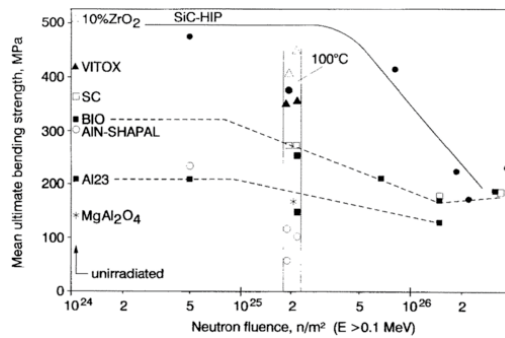

Fig. 32 Change in the bending stress α-Al₂O₃, MgAl₂O₄ and AlN irradiated with neutrons. Detail information for the specimens were described in a reference. Reproduced with permission from Dienst, W., 1994. J. Nucl. Mater. 211 (3), 186–193.

produce a disorder that can be described by the simple exchange of atoms within a discrete number of configurations. These modifications are generally quite drastic and above a given threshold, polytype or polymorph formation can no longer accommodate the disorder, and the mechanical properties of the systems can radically change, promoting a collapse of the usual structure and the appearance of glassy or amorphous phases with radically different dimensions and mechanical properties. Fluorites and a few other simple ionic systems seems to exhibit a strong resilience to those changes. Experimental techniques sensitive to different scales of order present in these materials can bring relevant information on the changes occurring in irradiated materials. This problem encompasses several length scales as short and long-range order are not unrelated in ionic systems. Some systems try to preserve the characteristics of their chemical bonds whereas others, like zirconium and uranium oxides, seem flexible enough to allow new and more complex atomic arrangements. Sometimes, these arrangements are inspired by polymorphism. In other systems the model seems to borrow from morphotropic phases because of the local stoichiometry changes induced by irradiation.

Depending on the energy necessary to create extended features, some systems like normal spinels seem to develop a response to the radiation damage that spans several unit cells, giving rise to mesoscopic structures that eventually coarsen to tartan-like phases. It seems quite possible then that the mechanical frustration of these mesoscale regions can trap the system in kinetically driven non-equilibrium configurations. This article tries to provide some elements to comprehend this complex problem that is a real bottleneck for experimental studies but also for numerical simulations and modeling.
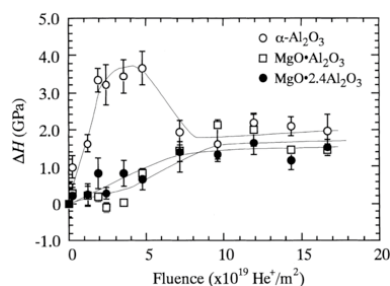
Fig. 33 Change in apparent hardness, ΔH, as a function of He ion fluence in α-Al$_2$O$_3$, stoichiometric and nonstoichiometric magnesium aluminate spinel (MgAl$_2$O$_4$ and MgO·2.4Al$_2$O$_3$) irradiated with 100 keV He ions at 300K. Reproduced with permission from Izumi, K., Yasuda, K., Kinoshita, C., Kutsuwada, M., 1998. J. Nucl. Mater. 258–263, 1856–1860.

References

1.. S.W. Gary, Fundamentals of Radiation Materials Science, Springer, Berlin, Heidelberg, 2013.
2.. M.A. Nastasi, J.W. Mayer, J.K. Hirvonen, Ion-Solid Interactions: Fundamentals and Applications, Cambridge University Press, 1996.
3.. N. Itoh, A.M. Stoneham, Radiat. Eff. Defects Solids 155 (1–4) (2001) 277–290.
4.. C.R.A. Catlow, A.M. Stoneham, J. Phys. C Solid State Phys. 16 (22) (1983) 4321–4338.
5.. L. Casillas-Trujillo, G. Baldinozzi, M.K. Patel, H. Xu, K.E. Sickafus, Phys. Rev. Mater. 1 (6) (2017), 065404.
6.. H.M. Naguib, R. Kelly, Radiat. Eff. 25 (1) (1975) 1–12.
7.. P.J. Burnett, T.F. Page, Radiat. Eff. 97 (3–4) (1986) 283–296.
8.. K. Trachenko, J. Phys. Condens. Matter 16 (2004), R1491.
9.. J.C. Bourgoin, Radiat. Eff. Defects Solids 111–112 (1–2) (1989) 29–36.
10.. K. Yasuda, T. Yamamoto, S. Seki, K. Shiiyama, S. Matsumura, Nucl. Instrum. Methods B 266 (12–13) (2008) 2834–2841.
11.. S.J. Zinkle, J. Nucl. Mater. 219 (1995) 113–127.
12.. S.J. Zinkle, C. Kinoshita, J. Nucl. Mater. 251 (1997) 200–217.
13.. C. Kinoshita, K. Yasuda, S. Matsumura, M. Shimada, Metall. Mater. Trans. A Phys. Metall. Mater. Sci. 35 A (8) (2004) 2257–2266.
14.. W.J. Weber, D.M. Duffy, L. Thomé, Y. Zhang, Curr. Opin. Solid State Mater. Sci 19 (1) (2015) 1–11.
15.. W.J. Weber, R.C. Ewing, C.R.A. Catlow, et al., J. Mater. Res. 13 (6) (1998) 1434–1484.
16.. F. Gao, H. Xiao, X. Zu, M. Posselt, W.J. Weber, Phys. Rev. Lett. 103 (2) (2009), 027405.
17.. R.S. Wilks, J. Nucl. Mater. 26 (2) (1968) 137–173.
18.. W. Dienst, J. Nucl. Mater. 191–194 (1992) 555–559.
19.. L.L. Snead, T. Nozawa, Y. Katoh, et al., J. Nucl. Mater. 371 (1–3) (2007) 329–377.
20.. T. Yano, J. Am. Ceram. Soc 82 (12) (1999) 3355–3364.
21.. W. Dienst, H. Zimmermann, J. Nucl. Mater. 212–215 (B) (1994) 1091–1095.
22.. P. Jung, A. Hishinuma, G.E. Lucas, H. Ullmaier, J. Nucl. Mater. 232 (2–3) (1996) 186–205.
23.. W.C. Oliver, G.M. Pharr, J. Mater. Res. 7 (6) (1992) 1564–1583.
24.. W.D. Nix, Metall. Trans. A 20 (11) (1989) 2217–2245.
25.. L.W. Hobbs, F.W. Clinard, S.J. Zinkle, R.C. Ewing, J. Nucl. Mater. 216 (1994) 291–321.
26.. R.C. Ewing, W.J. Weber, J. Lian, J. Appl. Phys. 95 (11) (2004) 5949–5971.
27.. Sickafus, K.E., Kotomin, E.A., Uberuaga, B.P., 2006. Radiation effects in solids. In: Proceedings of the NATO Advanced Study Institute the 32nd Course of the International School of Solid State Physics entitled Radiation Effects in Solids held in Erice, Sicily, Italy. July 17–29, 2004. Dordrecht: Springer.
28.. R.J.M. Konings, T.R. Allen, R.E. Stoller, S. Yamanaka, Material performance and corrosion/waste materials, In: R.J.M. Konings (Ed.), Comprehensive Nuclear Materials, 5, Elsevier, Spain, 2012.
29.. P. Vajda, J.-M. Costantini, Properties of Fluorite Structure Materials, Nova Science Publishers, 2013.
30.. D. Simeone, J.-M. Costantini, L. Luneville, et al., J. Mater. Res. 30 (9) (2015) 1495–1515.
31.. H. Akie, T. Muromura, H. Takano, S. Matsuura, Nucl. Technol. 107 (2) (1994) 182–192.
32.. C. Degueldre, T. Yamashita, J. Nucl. Mater. 319 (2003) 1–5.
33.. K.E. Sickafus, R.J. Hanrahan, K.J. McClellan, et al., Ceram. Soc. Bull. 78 (1999) 69.
34.. T. Yamashita, K. Kuramoto, N. Nitani, et al., J. Nucl. Mater. 320 (1–4) (2003) 126–132.
35.. R.J.M. Konings, K. Bakker, J.G. Boshoven, et al., J. Nucl. Mater. 274 (1–2) (1999) 84–90.
36.. T. Sonoda, M. Kinoshita, Y. Chimi, et al., Nucl. Instrum. Methods B 250 (1–2) (2006) 254–258.
37.. T. Sonoda, M. Kinoshita, N. Ishikawa, et al., Nucl. Instrum. Methods B 266 (12–13) (2008) 2882–2886.
38.. N. Ishikawa, K. Ohhara, Y. Ohta, O. Michikami, Nucl. Instrum. Methods B 268 (19) (2010) 3273–3276.
39.. B. Ye, M.A. Kirk, W. Chen, et al., J. Nucl. Mater. 414 (2) (2011) 251–256.

40.. M. Kinoshita, K. Yasunaga, T. Sonoda, et al., Nucl. Instrum. Methods B 267 (6) (2009) 960–963.
41.. A. Guglielmetti, A. Chartier, L. van Brutzel, et al., Nucl. Instrum. Methods B 266 (24) (2008) 5120–5125.
42.. D.S. Aidhy, D. Wolf, A. El-Azab, Scr. Mater. 65 (10) (2011) 867–870.
43.. K. Yasunaga, K. Yasuda, S. Matsumura, T. Sonoda, Nucl. Instrum. Methods B 266 (12–13) (2008) 2877–2881.
44.. J.-M. Costantini, G. Lelong, M. Guillaumet, et al., J. Phys. Condens. Matter. 28 (32) (2016) 325901.
45.. F.S. Galasso, Structure and Properties of Inorganic Solids, Pergamon Press, 1970.
46.. J.-M. Costantini, F. Beuneu, W.J. Weber, in: P. Vajda, J.-M. Costantini (Eds.), Chapter – 5 Radiation Damage in Cubic Stabilized Zirconia (ZrO$_{2-x}$) and Ceria (CeO$_{2-x}$), Nova Science Publishers, 2013, pp. 127–151.
47.. T. Wiss, R. Konings, in: P. Vajda, J.-M. Costantini (Eds.), Radiation Effects in Actinide Compounds with the Fluorite Structure, Nova Science Publishers, 2013, pp. 153–188.
48.. K. Nordlund, S.J. Zinkle, A.E. Sand, et al., J. Nucl. Mater. 512 (2018) 450–479.
49.. J. Soullard, E.A. Alamo, Radiat. Eff. 38 (3–4) (1978) 133–139.
50.. L. Van Brutzel, J.-M. Delaye, D. Ghaleb, M. Rarivomanantsoa, Philos. Mag. 83 (36) (2003) 4083–4101.
51.. C. Meis, A. Chartier, J. Nucl. Mater. 341 (1) (2005) 25–30.
52.. H.Y. Xiao, Y. Zhang, W.J. Weber, Phys. Rev. B. 86 (5) (2012) 054109.
53.. J.-M. Costantini, F. Beuneu, Phys. Status Solidi (c) 4 (3) (2007) 1258–1263.
54.. J.-M. Costantini, F. Beuneu, S. Morrison-Smith, R. Devanathan, W.J. Weber, J. Appl. Phys. 110 (12) (2011), 123506.
55.. A. Saiful Islam Bhuian, K. Kuwahara, T. Yamamoto, et al., Trans. Mater. Res. Soc. Jpn. 41 (3) (2016) 319–323.
56.. K. Shiiyama, T. Yamamoto, T. Takahashi, et al., Nucl. Instrum. Methods B 268 (19) (2010) 2980–2983.
57.. L. van Brutzel, A. Chartier, J.P. Crocombette, Phys. Rev. B. 78 (2) (2008) 024111.
58.. K. Yasuda, C. Kinoshita, S. Matsumura, A.I. Ryazanov, J. Nucl. Mater. 319 (2003) 74–80.
59.. O.S. Oen, Cross Sections for Atomic Displacements in Solids by Fast Electrons, Oak Ridge National Laboratory, Oak Ridge, TN, 1973.
60.. W.A. McKinley, H. Feshbach, Phys. Rev. 74 (12) (1948) 1759–1763.
61.. P.D. Lesueur, Philos. Mag. A 44 (4) (1981) 905–929.
62.. K.E. Sickafus, H. Matzke, T. Hartmann, et al., J. Nucl. Mater. 274 (1–2) (1999) 66–77.
63.. K. Yasuda, M. Nastasi, K.E. Sickafus, C.J. Maggiore, N. Yu, Nucl. Instrum. Methods B 136–138 (1998) 499–504.
64.. S. Moll, L. Thomé, G. Sattonnay, et al., J. Appl. Phys. 106 (7) (2009), 073509.
65.. L. Thomé, S. Moll, G. Sattonnay, et al., J. Nucl. Mater. 389 (2) (2009) 297–302.
66.. J. Jagielski, L. Thomé, Appl. Phys. A. 97 (1) (2009) 147–155.
67.. L.M. Wang, S.X. Wang, S. Zhu, R.C. Ewing, J. Nucl. Mater. 289 (1–2) (2001) 122–127.
68.. L. Vincent, L. Thorń, F. Garrido, O. Kaitasov, F. Houdelier, J. Appl. Phys. 104 (11) (2008), 114904.
69.. Y. Zhang, D.S. Aidhy, T. Varga, et al., Phys. Chem. Chem. Phys. 16 (17) (2014) 8051–8059.
70.. T. Hojo, H. Yamamoto, J. Aihara, et al., Nucl. Instrum. Methods B 241 (1–4) (2005) 536–542.
71.. J.-M. Costantini, F. Beuneu, J. Phys. Condens. Matter 23 (11) (2011), 115902.
72.. K. Yasunaga, K. Yasuda, S. Matsumura, T. Sonoda, Nucl. Instrum. Methods B 250 (1–2) (2006) 114–118.
73.. Watanabe, M., Noma, T., Yasuda, K., *et al.*, 2006. Proceedings of the 16th International Microscoipy Congress.
74.. S. Takaki, T. Yamamoto, M. Kutsuwada, K. Yasuda, S. Matsumura, Adv. Mater. Nucl. Energy 1514 (2013) 93.
75.. A.I. Ryazanov, K. Yasuda, C. Kinoshita, A.V. Klaptsov, J. Nucl. Mater. 323 (2–3) (2003) 372–379.
76.. J.-M. Costantini, N. Touati, L. Binet, et al., Philos. Mag. 98 (14) (2018) 1241–1255.
77.. T. Wiss, Chapter – 2.18 Radiation effects in UO$_2$, in: R.J.M. Konings (Ed.), Comprehensive Nuclear Materials, Elsevier Ltd, 2012, pp. 465–480.
78.. K. Yasuda, M. Etoh, K. Sawada, et al., Nucl. Instrum. Methods B 314 (2013) 185–190.
79.. S. Takaki, K. Yasuda, T. Yamamoto, S. Matsumura, N. Ishikawa, Nucl. Instrum. Methods B 326 (2014) 140–144.
80.. F. Garrido, S. Moll, G. Sattonnay, L. Thomé, L. Vincent, Nucl. Instrum. Methods B 267 (8–9) (2009) 1451–1455.
81.. T. Wiss, H. Matzke, C. Trautmann, M. Toulemonde, S. Klaumünzer, Nucl. Instrum. Methods B 122 (3) (1997) 583–588.
82.. J.-M. Costantini, S. Miro, G. Gutierrez, et al., J. Appl. Phys. 122 (20) (2017), 205901.
83.. K. Ohhara, N. Ishikawa, S. Sakai, et al., Nucl. Instrum. Methods B. 267 (2009) 973–975.
84.. G. Sattonnay, M. Lahrichi, A. Benyagoub, et al., Nucl. Instrum. Methods B 257 (1–2) (2007) 476–479.
85.. N. Ishikawa, T. Sonoda, T. Sawabe, H. Sugai, M. Sataka, Nucl. Instrum. Methods B 314 (2013) 180–184.
86.. N. Ishikawa, K. Takegahara, Nucl. Instrum. Methods B 272 (2012) 227–230.
87.. S. Takaki, K. Yasuda, T. Yamamoto, S. Matsumura, N. Ishikawa, Prog. Nucl. Energy. 92 (2016) 306–312.
88.. C. Dufour, A. Audouard, F. Beuneu, et al., J. Phys. Condens. Matter. 5 (26) (1993) 4573–4584.
89.. Lang, M. Comprehensive Nuclear Material, Elsevier.
90.. C.L. Tracy, M. Lang, J.M. Pray, et al., Nat. Commun. 6 (1) (2015) 6133.
91.. J.-M. Costantini, C. Trautmann, L. Thomé, J. Jagielski, F. Beuneu, J. Appl. Phys. 101 (7) (2007), 073501.
92.. H. Ohno, A. Iwase, D. Matsumura, et al., Nucl. Instrum. Methods B 266 (12–13) (2008) 3013–3017.
93.. A. Iwase, H. Ohno, N. Ishikawa, et al., Nucl. Instrum. Methods B 267 (6) (2009) 969–972.
94.. J.-M. Costantini, S. Miro, N. Touati, et al., J. Appl. Phys. 123 (2) (2018), 025901.
95.. J.-M. Costantini, F. Beuneu, Nucl. Instrum. Methods B 314 (2013) 130–134.
96.. J.-M. Costantini, F. Guillet, S. Lambert, et al., J. Appl. Phys. 104 (7) (2008), 073504.
97.. K. Nogita, K. Une, J. Nucl. Mater. 226 (3) (1995) 302–310.
98.. H. Matzke, J. Spino, J. Nucl. Mater. 248 (1997) 170–179.
99.. T. Sonoda, M. Kinoshita, I.L.F. Ray, et al., Nucl. Instrum. Methods B 191 (1–4) (2002) 622–628.
100..M. Weller, H. Schubert, J. Am. Ceram. Soc. 69 (7) (1986) 573–577.
101..E.H. Kisi, C.J. Howard, Key Eng. Mater. 153–154 (1998) 1–36.
102..G. Bernard-Granger, C. Guizard, S. Surblé, G. Baldinozzi, A. Addad, Acta Mater. 56 (17) (2008) 4658–4672.
103..E.C. Subbarao, H.S. Maiti, K.K. Srivastava, Phys. Status Solidi 21 (1) (1974) 9–40.
104..R.H. French, S.J. Glass, F.S. Ohuchi, Y.-N. Xu, W.Y. Ching, Phys. Rev. B. 49 (8) (1994) 5133–5142.
105..P. Bouvier, E. Djurado, G. Lucazeau, T. Le Bihan, Phys. Rev. B. 62 (13) (2000) 8731–8737.

106..R.C. Garvie, R.H. Hannink, R.T. Pascoe, Nature 258 (1975) 703–704.
107..P. Tolédano, V. Dmitriev, Reconstructive Phase Transitions, World Scientific, 1996.
108..A.A. Boulbitch, P. Tolédano, Phys. Rev. Lett. 81 (4) (1998) 838–841.
109..K. Negita, H. Takao, J. Phys. Chem. Solids 50 (3) (1989) 325–331.
110..D. Simeone, G. Baldinozzi, D. Gosset, et al., Phys. Rev. B 67 (6) (2003), 064111.
111..G. Baldinozzi, D. Simeone, D. Gosset, M. Dutheil, Phys. Rev. Lett. 90 (21) (2003), 216103.
112..A. Benyagoub, F. Levesque, F. Couvreur, et al., Appl. Phys. Lett. 77 (20) (2000) 3197–3199.
113..D. Simeone, D. Gosset, J.L. Bechade, A. Chevarier, J. Nucl. Mater. 300 (1) (2002) 27–38.
114..D. Simeone, G. Baldinozzi, D. Gosset, S. LeCaër, L. Mazerolles, Phys. Rev. B 70 (13) (2004) 134116.
115..J.A. Valdez, M. Tang, Z. Chi, M.I. Peters, K.E. Sickafus, Nucl. Instrum. Methods B 218 (2004) 103–110.
116..D. Simeone, G. Baldinozzi, D. Gosset, et al., Rev. Adv. Mater. Sci. 10 (2005) 118–122.
117..G. Baldinozzi, D. Simeone, D. Gosset, et al., Phys. Rev. B. 74 (13) (2006) 132107.
118..D. Simeone, G. Baldinozzi, D. Gosset, et al., Nucl. Instrum. Methods B 266 (12–13) (2008) 3023–3026.
119..R. Bullough, R.C. Newman, Reports Prog. Phys 33 (1) (1970) 303.
120..V.M. Orera, R.I. Merino, Y. Chen, R. Cases, P.J. Alonso, Phys. Rev. B 42 (16) (1990) 9782–9789.
121..A.S. Foster, V.B. Sulimov, F. Lopez Gejo, A.L. Shluger, R.M. Nieminen, Phys. Rev. B 64 (22) (2001), 224108.
122..J.-M. Costantini, A. Kahn-Harari, F. Beuneu, F. Couvreur, J. Appl. Phys. 99 (12) (2006), 123501.
123..J. Llopis, Phys. Status Solidi 119 (2) (1990) 661–667.
124..N.-D. Morelon, D. Ghaleb, J.-M. Delaye, L. Van Brutzel, Philos. Mag. 83 (13) (2003) 1533–1555.
125..B.P. Uberuaga, R. Smith, A.R. Cleave, et al., Phys. Rev. Lett. 92 (11) (2004) 115505.
126..S. Kartha, T. Castán, J.A. Krumhansl, J.P. Sethna, Phys. Rev. Lett. 67 (25) (1991) 3630–3633.
127..K.E. Sickafus, C. J. Wetteland, N. P. Baker, et al., Mater. Sci. Eng. A 253 (1–2) (1998) 78–85.
128..K.E. Sickafus, H. Matzke, K. Yasuda, et al., Nucl. Instrum. Methods B 141 (1–4) (1998) 358–365.
129..G. Sattonnay, S. Moll, V. Desbrosses, et al., Nucl. Instrum. Methods B 268 (19) (2010) 3040–3043.
130..K.E. Sickafus, C. J. Wetteland, N. P. Baker, et al., Mater. Sci. Eng. A 253 (1–2) (1998) 78–85.
131..R.J. McEachern, P. Taylor, J. Nucl. Mater. 254 (2–3) (1998) 87–121.
132..R.I. Cooper, B.T.M. Willis, Acta Cryst. 60 (4) (2004) 322–325.
133..L. Desgranges, G. Baldinozzi, G. Rousseau, J.-C. Nièpce, G. Calvarin, Inorg. Chem. 48 (16) (2009) 7585–7592.
134..L. Desgranges, G. Baldinozzi, MRS Proc. 1124 (2008), (1124-Q06-03-O07-03).
135..G. Baldinozzi, L. Desgranges, G. Rousseau, MRS Proc. 1215 (2009), (1215-V10-05).
136..D.A. Andersson, G. Baldinozzi, L. Desgranges, D.R. Conradson, S.D. Conradson, Inorg. Chem. 52 (5) (2013) 2769–2778.
137..L. Desgranges, Y. Ma, P. Garcia, et al., Inorg. Chem. 56 (1) (2017) 321–326.
138..A. Soulié, G. Baldinozzi, F. Garrido, J.-P. Crocombette, Inorg. Chem. 58 (19) (2019) 12678–12688.
139..G. Leinders, R. Delville, J. Pakarinen, et al., Inorg. Chem. 55 (19) (2016) 9923–9936.
140..L. Desgranges, G. Baldinozzi, D. Siméone, H.E. Fischer, Inorg. Chem 50 (13) (2011) 6146–6151.
141..L. Desgranges, G. Baldinozzi, P. Simon, G. Guimbretière, A. Canizares, J. Raman Spectrosc. 43 (3) (2012) 455–458.
142..G. Baldinozzi, L. Desgranges, D. Simeone, D. Gosset, L. Luneville, MRS Proc. 1383 (2012), (mrsf11-1383-a02-08).
143..L. Quémard, L. Desgranges, V. Bouineau, et al., J. Eur. Ceram. Soc. 29 (13) (2009) 2791–2798.
144..W.J. Weber, J. Nucl. Mater. 98 (1–2) (1981) 206–215.
145..T. Wiss, J.-P. Hiernaut, D. Roudil, et al., J. Nucl. Mater. 451 (1–3) (2014) 198–206.
146..H.J. Matzke, Radiat. Eff. 53 (3–4) (1980) 219–242.
147..D.R. Olander, P. Van Uffelen, J. Nucl. Mater. 288 (2–3) (2001) 137–147.
148..M. Tonks, D. Andersson, R. Devanathan, et al., J. Nucl. Mater. 504 (2018) 300–317.
149..V.V. Rondinella, T. Wiss, Mater. Today 13 (12) (2010) 24–32.
150..F. Cappia, D. Pizzocri, M. Marchetti, et al., J. Nucl. Mater. 479 (2016) 447–454.
151..J. Spino, J. Cobos-Sabate, F. Rousseau, J. Nucl. Mater. 322 (2–3) (2003) 204–216.
152..J. Noirot, L. Desgranges, J. Lamontagne, J. Nucl. Mater. 372 (2–3) (2008) 318–339.
153..T.J. Gerczak, C.M. Parish, P.D. Edmondson, C.A. Baldwin, K.A. Terrani, J. Nucl. Mater. 509 (2018) 245–259.
154..K. Hayashi, H. Kikuchi, K. Fukuda, J. Nucl. Mater. 248 (1997) 191–195.
155..P. Ruello, L. Desgranges, G. Baldinozzi, et al., J. Phys. Chem. Solids 66 (5) (2005) 823–831.
156..L. Desgranges, G. Baldinozzi, P. Ruello, C. Petot, J. Nucl. Mater. 420 (1–3) (2012) 334–337.
157..G. Baldinozzi, L. Desgranges, C. Petot, Nucl. Instrum. Methods B 327 (2014) 68–73.
158..R.J. Price, Nucl. Technol. 35 (2) (1977) 320–336.
159..M.K. Meyer, R. Fielding, J. Gan, J. Nucl. Mater. 371 (1–3) (2007) 281–287.
160..S.J. Zinkle, J.T. Busby, Mater. Today 12 (11) (2009) 12–19.
161..N.G. Wright, A.B. Horsfall, K. Vassilevski, Mater. Today 11 (1–2) (2008) 16–21.
162..J. Lamon, Chapter 2.12 – Properties and characteristics of SiC and SiC/SiC composites, in: R.J.M. Konings (Ed.), Comprehensive Nuclear Materials, Elsevier, 2012, pp. 323–338.
163..M. Bockstedte, A. Gali, A. Mattausch, O. Pankratov, J.W. Steeds, Phys. Status Solidi 245 (7) (2008) 1281–1297.
164..M. Ishimaru, I.-T. Bae, Y. Hirotsu, S. Matsumura, K.E. Sickafus, Phys. Rev. Lett. 89 (5) (2002), 055502.
165..W.J. Weber, Y. Zhang, L. Wang, Nucl. Instrum. Methods B 277 (2012) 1–5.
166..L.L. Snead, S.J. Zinkle, J.C. Hay, M.C. Osborne, Nucl. Instruments Methods Phys. Res. Sect. B Beam Interact. Mater. At. 141 (1–4) (1998) 123–132.
167..F. Gao, W.J. Weber, Phys. Rev. B. 66 (2) (2002), 024106.
168..X. Kerbiriou, J.-M. Costantini, M. Sauzay, et al., J. Appl. Phys. 105 (7) (2009), 073513.
169..J.-M. Costantini, X. Kerbiriou, M. Sauzay, L. Thomé, J. Phys. D Appl. Phys. 45 (46) (2012), 465301.
170..S. Miro, J.-M. Costantini, J. Huguet-Garcia, L. Thomé, Recrystalization of hexagonal silicon carbide after gold ion irradiation and thermal annealing, Philos. Mag. 94 (34) (2014) 3898–3913.
171..W. Jiang, Y. Zhang, W.J. Weber, Phys. Rev. B 70 (16) (2004), 165208.

172. V. Heera, F. Prokert, N. Schell, et al., Appl. Phys. Lett. 70 (26) (1997) 3531–3533.
173. W. Jiang, C.M. Wang, W.J. Weber, M.H. Engelhard, L.V. Saraf, J. Appl. Phys. 95 (9) (2004) 4687–4690.
174. R. Devanathan, F. Gao, W.J. Weber, Appl. Phys. Lett. 84 (19) (2004) 3909–3911.
175. N. Swaminathan, D. Morgan, I. Szlufarska, J. Nucl. Mater. 414 (3) (2011) 431–439.
176. E. Jin, L.-S. Niu, Phys. B Condens. Matter 406 (3) (2011) 601–608.
177. E.Z. Jin, L.S. Niu, Vacuum 86 (7) (2012) 917–923.
178. X. Yuan, L.W. Hobbs, Nucl. Instrum. Methods B 191 (1–4) (2002) 74–82.
179. W.J. Weber, F. Gao, Irradiation-induced defect clustering and amorphization in silicon carbide, J. Mater. Res. 25 (12) (2010) 2349–2353.
180. F. Gao, W.J. Weber, Phys. Rev. B 69 (22) (2004), 224108.
181. L.L. Snead, J.C. Hay, J. Nucl. Mater. 273 (2) (1999) 213–220.
182. R. Devanathan, W.J. Weber, J. Nucl. Mater. 278 (2000) 258–265.
183. J.M. Perlado, L. Malerba, A. Sánchez-Rubio, T. Díaz de la Rubia, J. Nucl. Mater. 276 (1–3) (2000) 235–242.
184. L. Malerba, J.M. Perlado, Phys. Rev. B 65 (4) (2002), 045202.
185. G. Lucas, L. Pizzagalli, Nucl. Instrum. Methods B 229 (3–4) (2005) 359–366.
186. F. Gao, W.J. Weber, R. Devanathan, Nucl. Instrum. Methods B 191 (2002) 487–496.
187. W. Jiang, W.J. Weber, S. Thevuthasan, D.E. McCready, Nucl. Instrum. Methods B 148 (1–4) (1999) 557–561.
188. J. Lefèvre, J.-M. Constantini, S. Esnouf, G. Petite, J. Appl. Phys. 105 (2) (2009), 023520.
189. M. Hundhausen, R. Püsche, J. Röhrl, L. Ley, Phys. Status Solidi 245 (7) (2008) 1356–1368.
190. K. Karch, P. Pavone, W. Windl, O. Schütt, D. Strauch, Phys. Rev. B 50 (23) (1994) 17054–17063.
191. B. Dorner, H. Schober, A. Wonhas, M. Schmitt, D. Strauch, Eur. Phys. J. B 5 (4–6) (1998) 839–846.
192. J. Serrano, J. Strempfer, M. Cardona, et al., Appl. Phys. Lett. 80 (23) (2002) 4360–4362.
193. G. Nilsson, G. Nelin, Phys. Rev. B 6 (10) (1972) 3777–3786.
194. M. Holt, Z. Wu, H. Hong, et al., Phys. Rev. Lett. 83 (16) (1999) 3317–3319.
195. S.R. Elliott, Physics of Amorphous Materials, second ed., Longman Scientific & Technical, New York, 1983.
196. R. Zallen, The Physics of Amorphous Solids, John Wiley & Sons, New York, 1983.
197. T. Kimoto, A. Itoh, H. Matsunami, T. Nakata, M. Watanabe, J. Electron. Mater. 25 (5) (1996) 879–884.
198. S. Sorieul, J.-M. Constantini, L. Gosmain, L. Thomé, J.-J. Grob, J. Phys. Condens. Matter 18 (22) (2006) 5235–5251.
199. P.F. Wang, L. Huang, W. Zhu, Y.F. Ruan, Solid State Commun. 152 (10) (2012) 887–890.
200. T. Koyanagi, M.J. Lance, Y. Katoh, Scr. Mater. 125 (2016) 58–62.
201. F. Linez, A. Canizares, A. Gentils, et al., J. Raman Spectrosc. 43 (7) (2012) 939–944.
202. J.-M. Costantini, S. Miro, O. Pluchery, J. Phys. D Appl. Phys. 50 (9) (2017), 095301.
203. V.I. Ivashchenko, P.E.A. Turchi, V.I. Shevchenko, L.A. Ivashchenko, G.V. Rusakov, Phys. Rev. B 66 (19) (2002), 195201.
204. M. Bertolus, F. Finocchi, P. Millié, J. Chem. Phys. 120 (9) (2004) 4333–4343.
205. W. Bolse, Nucl. Instrum. Methods B 141 (1–4) (1998) 133–139.
206. S. Sorieul, J.-M. Constantini, L. Gosmain, et al., J. Phys. Condens. Matter. 18 (37) (2006) 8493–8502.
207. M.C. Ridgway, G. d.M. Azevedo, C.J. Glover, K.M. Yu, G. Foran, J. Nucl. Instrum. Methods B 199 (2003) 235–239.
208. G. de M. Azevedo, C.J. Glover, M.C. Ridgway, K.M. Yu, G.J. Foran, Phys. Rev. B 68 (11) (2003), 115204.
209. R. Menzel, K. Gärtner, W. Wesch, H. Hobert, J. Appl. Phys. 88 (10) (2000) 5658–5661.
210. A. Pérez-Rodríguez, Y. Pacaud, L. Calvo-Barrio, et al., J. Electron. Mater. 25 (3) (1996) 541–547.
211. S. Sorieul, X. Kerbiriou, J.-M. Constantini, et al., J. Phys. Condens. Matter 24 (12) (2012), 125801.
212. M.H. Brodsky, M. Cardona, J. Non. Cryst. Solids 31 (1–2) (1978) 81–108.
213. J. Tauc, Infrared and raman spectroscopy of amorphous semiconductors, in: S.S. Mitra (Ed.), Physics of Structurally Disordered Solids, Springer, Boston, MA, 1976, pp. 525–540.
214. F. Finocchi, G. Galli, M. Parrinello, C.M. Bertoni, Phys. Rev. Lett. 68 (20) (1992) 3044–3047.
215. R. Devanathan, F. Gao, W.J. Weber, Nucl. Instrum. Methods B 255 (1) (2007) 130–135.
216. K. Xue, L.-S. Niu, H.-J. Shi, J. Appl. Phys. 104 (5) (2008) 053518.
217. T.R. Allen, G.S. Was, Radiation-enhanced diffusion and radiation-induced segregation, in: K.E. Sickafus, E.A. Kotomin, B.P. Uberuaga (Eds.), Radiation Effects in Solids, Springer Netherlands, Dordrecht, 2007, pp. 123–151.
218. S. Muto, T. Tanabe, J. Appl. Phys. 93 (7) (2003) 3765–3775.
219. M. Ishimaru, A. Hirata, M. Naito, et al., J. Appl. Phys. 104 (3) (2008), 033503.
220. J. Tersoff, Phys. Rev. B 49 (23) (1994) 16349–16352.
221. S. Pascarelli, F. Boscherini, S. Mobilio, F. Evangelisti, Phys. Rev. B 45 (4) (1992) 1650–1654.
222. G. Roma, Phys. Status Solidi 213 (11) (2016) 2995–2999.
223. H.D. Lutz, H. Haeuseler, J. Mol. Struct. 511–512 (1999) 69–75.
224. E. Wendler, A. Heft, U. Zammit, et al., Nucl. Instrum. Methods B 116 (1–4) (1996) 398–403.
225. R.J. Price, Nucl. Technol. 35 (2) (1977) 320–336.
226. C.H. Wu, J.P. Bonal, B. Kryger, J. Nucl. Mater. 208 (1–2) (1994) 1–7.
227. Y. Katoh, H. Kishimoto, A. Kohyama, J. Nucl. Mater. 307–311 (2) (2002) 1221–1226.
228. I. Szlufarska, R.K. Kalia, A. Nakano, P. Vashishta, Appl. Phys. Lett. 86 (2) (2005), 021915.
229. I. Szlufarska, R.K. Kalia, A. Nakano, P. Vashishta, Appl. Phys. Lett. 85 (3) (2004) 378–380.
230. S. Miro, J.-M. Constantini, S. Sorieul, L. Gosmain, L. Thomé, Philos. Mag. Lett. 92 (11) (2012) 633–639.
231. P. Musumeci, R. Reitano, L. Calcagno, et al., Philos. Mag. B 76 (3) (1997) 323–333.
232. K. Wang, W.G. Spitzer, G.K. Hubler, D.K. Sadana, J. Appl. Phys. 58 (12) (1985) 4553–4564.
233. L.L. Snead, S. Zinkle, J. Nucl. Instrum. Methods B 191 (1–4) (2002) 497–503.
234. S. Inoue, K. Yoshii, M. Umeno, H. Kawabe, Thin Solid Films 151 (3) (1987) 403–412.
235. L. Calcagno, P. Musumeci, F. Roccaforte, C. Bongiorno, G. Foti, Appl. Surf. Sci. 184 (1–4) (2001) 123–127.
236. K. Xue, L.-S. Niu, H.-J. Shi, J. Liu, Thin Solid Films 516 (12) (2008) 3855–3861.
237. S.J. Zinkle, V.A. Skuratov, D.T. Hoelzer, Nucl. Instrum. Methods B 191 (1–4) (2002) 758–766.

238..Y. Zhang, R. Sachan, O.H. Pakarinen, et al., Nat. Commun. 6 (1) (2015), 8049.
239..M. Backman, M. Toulemonde, O.H. Pakarinen, et al., Comput. Mater. Sci. 67 (2013) 261–265.
240..A. Benyagoub, A. Audren, L. Thomé, F. Garrido, Appl. Phys. Lett. 89 (24) (2006) 241914.
241..Y. Zhang, H. Xue, E. Zarkadoula, et al., Curr. Opin. Solid State Mater. Sci. 21 (6) (2017) 285–298.
242..A. Debelle, M. Backman, L. Thomé, et al., Nucl. Instrum Methods B 326 (2014) 326–331.
243..W. Jiang, H. Wang, I. Kim, Y. Zhang, W.J. Weber, J. Mater. Res. 25 (12) (2010) 2341–2348.
244..K. Imada, M. Ishimaru, K. Sato, et al., J. Nucl. Mater. 465 (2015) 433–437.
245..K. Imada, M. Ishimaru, H. Xue, et al., J. Nucl. Mater. 478 (2016) 310–314.
246..F. Gao, D. Chen, W. Hu, W.J. Weber, Phys. Rev. B. 81 (18) (2010), 184101.
247..A.G. Perez-Bergquist, T. Nozawa, C. Shih, et al., J. Nucl. Mater. 462 (2015) 443–449.
248..J. Huguet-Garcia, A. Jankowiak, S. Miro, et al., EPJ Nucl. Sci. Technol. 1 (2015) 8.
249..J. Huguet-Garcia, A. Jankowiak, S. Miro, et al., Phys. Status Solidi 252 (1) (2015) 149–152.
250..J. Huguet-Garcia, A. Jankowiak, S. Miro, et al., J. Mater. Res. 30 (9) (2015) 1572–1582.
251..A. Jankowiak, C. Grygiel, I. Monnet, et al., Nucl. Instrum. Methods B 314 (2013) 144–148.
252..K.E. Sickafus, J.M. Wills, N.W. Grimes, J. Am. Ceram. Soc. 82 (12) (1999) 3279–3292.
253..C. Degueldre, J.M. Paratte, J. Nucl. Mater. 274 (1–2) (1999) 1–6.
254..T. Yamashita, K. Kuramoto, H. Akie, et al., J. Nucl. Sci. Technol. 39 (8) (2002) 865–871.
255..S. Yamamoto, L. de Kock, V. Belyakov, et al., Irradiation tests on ITER diagnostic components, in: P.E. Stott, G. Gorini, P. Prandoni, E. Sindoni, et al. (Eds.), Diagnostics for Experimental Thermonuclear Fusion Reactors 2, Springer US, Boston, MA, 1998, pp. 269–278.
256..T. Shikama, K. Yasuda, S. Yamamoto, et al., J. Nucl. Mater. 271–272 (1999) 560–568.
257..K.E. Sickafus, Comprehensive Nuclear Materials, Elsevier, Spain, 2012123–139.
258..C. Kinoshita, Microstructural evolution of irradiated ceramics, in: K.E. Sickafus, E.A. Kotomin, B.P. Uberuaga (Eds.), Radiation Effects in Solids, Springer Netherlands, Dordrecht, 2007, pp. 193–232.
259..Y. Kazuhiro, C. Kinoshita, S. Matsumura, Defect Diffus. Forum. 206–207 (2002) 53–74.
260..C. Kinoshita, K. Nakai, Jpn. J. Appl. Phys. 2 (1989) 105.
261..C. Kinoshita, K. Fukumoto, K. Fukuda, F.A. Garner, G.W. Hollenberg, J. Nucl. Mater. 219 (1995) 143–151.
262..K. Fukumoto, C. Kinoshita, F.A. Garner, J. Nucl. Sci. Technol. 32 (8) (1995) 773–778.
263..K.E. Sickafus, A.C. Larson, N. Yu, et al., J. Nucl. Mater. 219 (1995) 128–134.
264..S. Zinkle, J. Radiat. Eff. Defects Solids 148 (1–4) (1999) 447–477.
265..K. Yasuda, C. Kinoshita, R. Morisaki, H. Abe, Philos. Mag. A 78 (3) (1998) 583–598.
266..J.C. Bourgoin, J.W. Corbett, Radiat. Eff. 36 (3–4) (1978) 157–188.
267..E.A. Kotomin, A.I. Popov, Nucl. Instrum. Methods B 141 (1–4) (1998) 1–15.
268..R.E. Williford, R. Devanathan, W.J. Weber, Nucl. Instrum. Methods B 141 (1–4) (1998) 94–98.
269..R. Smith, D. Bacorisen, B.P. Uberuaga, et al., J. Phys. Condens. Matter. 17 (6) (2005) 875–891.
270..G.P. Summers, G.S. White, K.H. Lee, J.H. Crawford, Phys. Rev. B. 21 (6) (1980) 2578–2584.
271..J.-M. Costantini, G. Lelong, M. Guillaumet, S. Takaki, K. Yasuda, J. Appl. Phys. 124 (24) (2018), 245901.
272..K. Yasuda, C. Kinoshita, Nucl. Instrum. Methods B 191 (1–4) (2002) 559–564.
273..C. Kinoshita, S. Matsumura, K. Yasuda, T. Soeda, M. Noujima, MRS Proc. 540 (1998) 287.
274..F.W. Clinard, G.F. Hurley, L.W. Hobbs, J. Nucl. Mater. 108–109 (1982) 655–670.
275..C.A. Parker, L.W. Hobbs, K.C. Russell, F.W. Clinard, J. Nucl. Mater. 133–134 (1985) 741–744.
276..R.A. Youngman, T.E. Mitchell, F.W. Clinard, G.F. Hurley, J. Mater. Res. 6 (10) (1991) 2178–2187.
277..K. Yasuda, C. Kinoshita, K. Fukuda, F.A. Garner, J. Nucl. Mater. 283–287 (2000) 937–941.
278..N. Yu, K.E. Sickafus, M. Nastasi, First observation of amorphization in single-crystal MgAL$_2$O$_4$ spinel, Philos. Mag. Lett. 70 (4) (1994) 235–240.
279..K.E. Sickafus, N. Yu, M.J. Nastasi, Nucl. Mater. 304 (2–3) (2002) 237–241.
280..L. Wang, W. Gong, S. Wang, R.C. Ewing, J. Am. Ceram. Soc. 82 (12) (1999) 3321–3329.
281..R. Devanathan, K.E. Sickafus, N. Yu, M. Nastasi, Philos. Mag. Lett. 72 (3) (1995) 155–161.
282..D. Simeone, C. Dodane-Thiriet, D. Gosset, P. Daniel, M. Beauvy, J. Nucl. Mater. 300 (2–3) (2002) 151–160.
283..G. Baldinozzi, D. Simeone, D. Gosset, et al., Nucl. Instrum. Methods B 266 (12–13) (2008) 2848–2853.
284..M. Ishimaru, Y. Hirotsu, I.V. Afanasyev-Charkin, K.E. Sickafus, J. Phys. Condens. Matter 14 (2002) 1237–1247.
285..T. Soeda, S. Matsumura, C. Kinoshita, N.J. Zaluzec, J. Nucl. Mater. 283–287 (2000) 952–956.
286..T. Sawabe, T. Yano, J. Nucl. Mater. 373 (1–3) (2008) 328–334.
287..L. Thomé, A. Gentils, J. Jagielski, F. Garrido, T. Thomé, Vacuum 81 (10) (2007) 1264–1270.
288..A. Chartier, T. Yamamoto, K. Yasuda, C. Meis, S. Matsumura, J. Nucl. Mater. 378 (2) (2008) 188–192.
289..T. Yamamoto, A. Chartier, K. Yasuda, et al., Nucl. Instrum. Methods B 266 (12–13) (2008) 2676–2682.
290..C. Liu, Y. Li, T. Shi, Q. Peng, F. Gao, J. Nucl. Mater (2019)527.
291..S.P. Chen, M. Yan, J.D. Gale, et al., Philos. Mag. Lett. 73 (2) (1996) 51–62.
292..S.J. Zinkle, H. Matzke, V.A. Skuratov, MRS Proc. 540 (1998) 299.
293..B.P. Uberuaga, M. Tang, C. Jiang, et al., Nat. Commun. 6 (2015).
294..S.J. Zinkle, V.A. Skuratov, Nucl. Instrum. Methods B 141 (1–4) (1998) 737–746.
295..T. Yamamoto, M. Shimada, K. Yasuda, et al., Nucl. Instrum. Methods B 245 (1) (2006) 235–238.
296..K. Yasuda, T. Yamamoto, M. Shimada, et al., Nucl. Instrum. Methods B 250 (1–2) (2006) 238–244.
297..K. Yasuda, T. Yamamoto, M. Syo, JOM 59 (4) (2007) 27–30.
298..K. Yasuda, T. Yamamoto, M. Etoh, et al., Int. J. Mater. Res. 102 (9) (2011) 1082–1088.
299..S. Yoshioka, K. Tsuruta, T. Yamamoto, et al., Phys. Chem. Chem. Phys. 20 (7) (2018) 4962–4969.
300..T. Aruga, Y. Katano, T. Ohmichi, S. Okayasu, Y. Kazumata, Nucl. Instrum. Methods B 166–167 (2000) 913–919.
301..Y.G. Chukalkin, V.V. Petrov, V.R. Shtirts, B.N. Goshchitskii, Phys. Status Solidi 92 (2) (1985) 347–354.
302..G. Baldinozzi, D. Simeone, D. Gosset, et al., Nucl. Instrum. Methods B 250 (1–2) (2006) 119–122.
303..R.J.D. Tilley, Nature 269 (5625) (1977) 229–231.

304..J.S. Anderson, B.G. Hyde, J. Phys. Chem. Solids 28 (8) (1967) 1393–1408.
305..R.B. Neder, F. Frey, H. Schulz, Acta Cryst. 46 (10) (1990) 792–798.
306..G.F. Hurley, J.C. Kennedy, F.W. Clinard, R.A. Youngman, W.R. McDonell, J. Nucl. Mater. 103 (C) (1981) 761–765.
307..C. Hazelton, J. Rice, L.L. Snead, S.J. Zinkle, J. Nucl. Mater. 253 (1–3) (1998) 190–195.
308..W. Dienst, J. Nucl. Mater. 211 (3) (1994) 186–193.
309..F.W. Clinard, W. Dienst, E.H. Farnum, J. Nucl. Mater. 212–215 (1994) 1075–1080.
310..W. Dienst, J. Nucl. Mater. 191–194 (1992) 555–559.
311..S.J. Zinkle, J. Am. Ceram. Soc. 72 (8) (1989) 1343–1351.
312..K. Izumi, K. Yasuda, C. Kinoshita, M. Kutsuwada, J. Nucl. Mater. 258–263 (1998) 1856–1860.
313..J. Jagielski, L. Thomé, P. Aubert, et al., Vacuum 83 (2009) S9–S12.
314..J. Jagielski, P. Aubert, O. Maciejak, et al., Nucl. Instrum. Methods B 286 (2012) 196–199.